LITHOS 456-457 (2023) 107306

Contents lists available at ScienceDirect

LITHOS

journal homepage: www.elsevier.com/locate/lithos

Geochemical diversity and tectonic relationships in monogenetic volcanic fields: A case study of the Sredinny Range, Kamchatka

Anna O. Volynets [a,*], Nikolai Nekrylov [a,b,c], Natalia Gorbach [a], Georgy Ovsyannikov [a,d], Maria Tolstykh [e], Maria Pevzner [f], Egor Zelenin [f], Vasily Shcherbakov [d], Vladimir Lebedev [g], Anastasia Plechova [e], Andrey Babansky [g]

[a] Institute of Volcanology and Seismology, Far East Branch of the Russian Academy of Sciences, bul'v. Piipa 9, Petropavlovsk-Kamchatsky 683006, Russia
[b] Fersman Mineralogical Museum, Leninskiy av., 18/2, Moscow 115162, Russia
[c] Institute of Geological Sciences, Armenian National Academy of Sciences, 24a Marshal Baghramyan Ave, Yerevan 0019, Armenia
[d] Moscow State University, Geological Department, Vorobievy Gory 1, Moscow, Russia
[e] Vernadsky Institute of Geochemistry and Analytical Chemistry, Russian Academy of Sciences, ul. Kosygina 19, Moscow 119091, Russia
[f] Geological Institute, Russian Academy of Sciences, Pyzhevskii per. 7, Moscow 119017, Russia
[g] Institute of Geology of Ore Deposits, Petrography, Mineralogy and Geochemistry, Russian Academy of Sciences, Staromonetny per. 35, Moscow 119017, Russia

ARTICLE INFO

Keywords:
Kamchatka
Sredinny Range
High-Mg rocks
Faults
Subduction zone
LREE

ABSTRACT

We report, here, the composition and K—Ar ages of a representative collection of volcanic rocks that erupted within three monogenetic volcanic fields in the active fault zone of the Sredinny Range of Kamchatka: Tigilsky Dol, Mount Oxi massif and Anaunsky Dol. The studied rocks display a wide range of compositions (medium-K, moderate-Mg, high-K, high-Ti and high-Mg basalts, and high-LREE picrobasalts); the high-Mg varieties are confined to faults. Five main periods of volcanic activity were investigated, 4.3–3, 2, 1.5, 1 Ma and from 0.3 to <0.05 Ma. Primitive lavas first emerged on the surface at 3.5 Ma. There was a massive outpouring of high-Mg lavas at 1.5–1 and 0.3 Ma, which could have been related to the formation of the fault zone. This is the first report of rocks in Kamchatka with a high-LREE picrobasaltic composition (1.5 Ma). The Fo content of the olivine phenocrysts reaches 93.2 mol%, which is the highest value known for Quaternary Kamchatka basalts. A very heterogeneous source, even for individual eruptions is indicated by the minor element contents in the olivine (Ni, Mn and Ca); Cr-spinel – olivine paragenesis show that all the rocks studied crystallized in the same temperature range (1111–1292 °C), whereas the oxygen fugacity for the different samples varied from ΔQFM +0.7 to +2.0 log. units. A melt inclusion study showed that the Mg basalts of the Mt. Oxi massif and the high-LREE picrobasalts of Tigilsky Dol had different fluid sources that were enriched and depleted in water and Cl, respectively. We argue that the fluid source for the Mt. Oxi massif was likely the remains of the Pacific slab under the Sredinny Range, whereas, for the high-LREE picrobasalts of Tigilsky Dol, it was the lithospheric lithologies. The low content of S and high content of Cu in the oxidized high-LREE basalts provide additional evidence that they originated from the re-melting of sulfur-poor lithospheric lithologies. Both the fault zone and the lithosphere re-activation in the region are likely linked to the regional stress field.

1. Introduction

The Kamchatka volcanic arc is a long-lived subduction system situated in the northwestern portion of the Pacific Ring of Fire. It has a complex geological history and is located at the triple-junction of the Pacific, Bering Sea and Eurasian plates. There are three volcanic zones in Kamchatka, running parallel to the trench: the Eastern Volcanic Front (EVF), the Central Kamchatka Depression (CKD), and the Sredinny Range (SR), which is situated in the back-arc. The active Benioff zone is located beneath the volcanoes of the EVF and CKD at depths ranging from approximately 100 to 180 km. Under the SR, the slab has been imaged seismically in the southern part – at ~400 km depth beneath the Khangar volcano and at ~300 km depth beneath the volcanoes of the eastern flank of the SR, up to the latitude of the Bystraya river (Gorbatov et al., 1997; Fig. 1). Also, according to Zhao et al. (2021), it is present at a depth of approximately 200 km along the eastern foot of the SR main

* Corresponding author.
E-mail addresses: a.volynets@gmail.com, volynets@kscnet.ru (A.O. Volynets).

https://doi.org/10.1016/j.lithos.2023.107306
Received 5 May 2023; Received in revised form 28 July 2023; Accepted 29 July 2023
Available online 1 August 2023

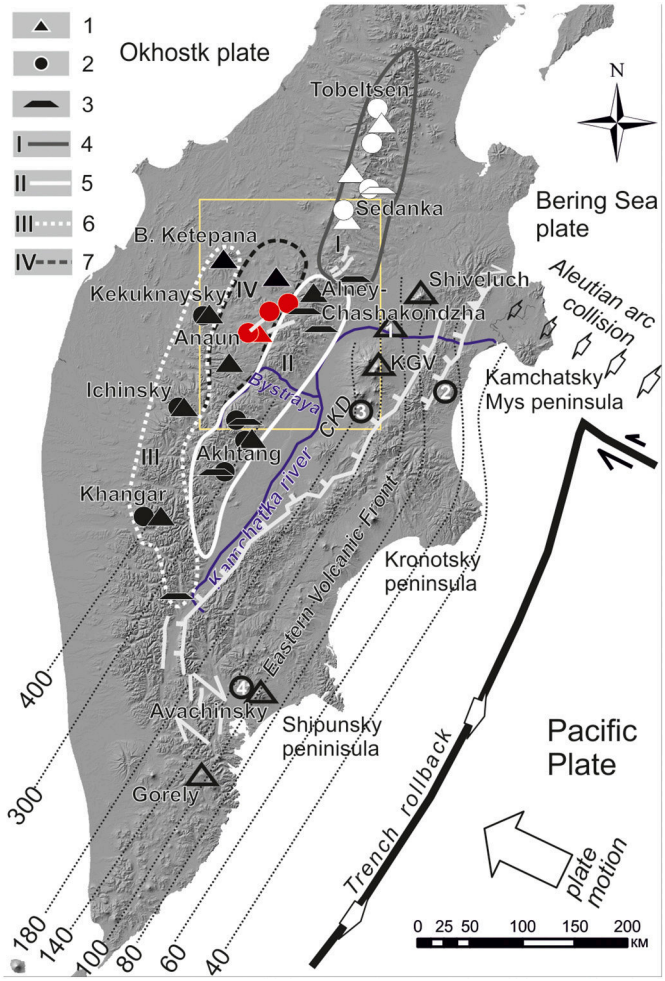

Fig. 1. A schematic map of Kamchatka, showing the location of the Sredinny Range, sampling sites and other objects mentioned in the text. Legend: 1 – stratovolcanoes, 2 – monogenetic volcanic fields, 3 – plateau, 4–7 – the division of the SR according to (Volynets et al., 2018): 4 – northern part, 5–7 – southern part: 5 – "eastern" flank, 6 – "western" flank, 7 – "central" flank. Red symbols – objects of this study; black – volcanic edifices from the southern part of the SR, white – from the northern part of the SR; unfilled – volcanoes from CKD and EVF. 1 – Kharchinsky volcano, 2 – cones in the Azhabachye lake area, 3 – Tolbachinsky Dol; 4 – Mt. Medvezh'ya near Koryaksky volcano. KGV – the Klyuchevskaya group of volcanoes. The thin dotted lines with numbers denote the depth contours of the upper boundary of the subducting Pacific slab (Gorbatov et al., 1997). Faults are shown with black lines with hatches for normal faults, triangles for reverse and thrust faults, and one-sided arrows for strike-slip faults. The yellow rectangular outline corresponds to the inset in Fig. 2. Note the location of the studied site above the northern end of the subducting Pacific slab. For the interpretation of the colour of symbols hereafter, the reader is referred to the web version of the article. (For interpretation of the references to colour in this and other figures legends, the reader is referred to the web version of this article.)

watershed, up to the latitude of the Shiveluch volcano (Fig. 1). In the Miocene, the Pacific plate was subducted roughly 200 km to the west of its current position, and the SR served as a volcanic front for this subduction (e.g. Avdeiko et al., 2006; Konstantinovskaia, 2001). Between 10 and 2 Ma, the front of subduction moved to the east to its present position due to the gradual accretion of the extinct Kronotsk arc terranes (which are now represented by the eastern peninsulas – Shipunsky, Kronotsky and Kamchatsky Mys, Fig. 1), and the SR now represents the back-arc part of the contemporary active continental margin (Avdeiko et al., 2006; Lander and Shapiro, 2007; Volynets, 1994). Since the docking of the Kronotsky arc approximately 10–2 Ma (Lander and Shapiro, 2007), Kamchatka has been stretching oceanward (Kozhurin and Zelenin, 2017) due to slab rollback (Schellart et al., 2007).

For many years, volcanism in the SR was considered to have ceased, but tephrochronological studies over the last 20 years have shown that numerous Holocene eruptions have taken place from the south (Khangar volcano, 54.761° N, 157.411° E) to the north (Tobeltsen cone, 58.259° N, 160.730° E) of the Range (Bazanova and Pevzner, 2001; Dirksen, 2009; Pevzner, 2004, 2015). The Sredinny Range has a wide distribution of monogenetic volcanic fields (MVFs) with over 1000 scoria cones covering an area of about 8500 km^2 (Laverov, 2005; Ogorodov et al., 1972). Németh and Kereszturi (2015) emphasized several main features that distinguish MVFs including the polymagmatic origin of the eruptive centers. That may be manifested by the eruption of magmas with contrasting chemical compositions (within a single event or as separate eruptive episodes in the same MVF). Several examples of compositionally heterogeneous monogenetic fields have been reported from around the world (e.g., Awdankiewicz et al., 2016; Rasoazanamparany et al., 2015; Smith et al., 2021; Uslular and Gençalioğlu-Kuşcu, 2019). These monogenetic fields typically consist of alkaline or high-Mg rocks, which preserve signs of small-scale mantle heterogeneity in their composition. Other features of MVFs include the large volume of some edifices and clustering of monogenetic edifices due probably to the existence of long-lived and complicated magmatic plumbing systems under MVFs and the absence of a focused central feeding vent. Monogenetic volcanic fields are commonly situated in areas with faults and their clusters, which could be attributed to the specific geometry of the magmatic chambers and the structures of the magma plumbing systems in the crust. As noted by Connor et al. (2000), ascending magmas exploit preexisting structures repeatedly during separate episodes of activity. Le Corvec et al. (2013) argued that the spatial distribution of the volcanic centers in volcanic fields results from an interplay between deep-level influences (i.e., the nature of the magma source) and shallow-level influences (i.e., the stress field and pre-existing crustal structures) of the lithosphere. Therefore, an investigation of MVFs associated with fault systems could provide insight into the processes governing the initiation and evolution of distributed volcanism.

This work is the first to examine a poorly studied area of the Sredinny Range. It is the area where active faulting within the back-arc region of a contemporary subduction zone is coupled with a wide distribution of monogenetic volcanoes. We present new data on the geochemistry, mineralogy and olivine-hosted melt inclusions of the volcanic rocks that erupted along the fault zone (FZ), focus on their unusual position, and discuss how the system of active faults might affect the initiation and evolution of this MVF.

2. Geological setting and sampling

From a geomorphological and geochemical point of view, the SR can be divided into two parts – northern and southern (Fig. 1). The northern part, which stretches to the NE from the latitude of the Alney-Chashakondzha massif is a narrow ridge. The southern part is much wider, up to 120 km wide, and consists of three flanks: "western" (from Khangar to the Bolshaya Ketepana volcanic massif), "eastern" (the main watershed of the SR up to the Alney massif), and "central" (located between the western and eastern flanks). Geochemical and isotopic features of the erupted rocks confirm this subdivision (Volynets et al., 2018). Within the northern SR, typical island-arc rocks erupted in the Miocene, and rocks with transitional (which combine elevated fluid-mobile element concentrations with substantial enrichment by all HFSE) composition – in the Pliocene-Quaternary. Within the southern part, a transitional type of rock is usual for the "western" flank, whereas the "eastern" and "central" flanks are characterized by island-arc type rocks of both Miocene and Pliocene-Quaternary age, and the degree of HFSE enrichment in the younger rocks is much less than in other parts of the SR.

At the location of this geomorphological transition between northern

and southern parts of the SR, a large SW-NE fault zone crosses the main watershed of the Sredinny Range at an azimuth of 40° (inset in Fig. 2; Krykun et al., 2020; Zelenin and Garipova, 2022). The total deformation zone extends for 250 km and has an average width of ~40 km. Our research area coincides with the southern part of this zone, with a strike of 30–35°, forming a belt approximately 70 km long and 10–15 km wide, stretching between Chashakondzha and Anaun volcanoes (Fig. 2). Further to the north, the fault zone shifts eastward from the volcanic zone and dies out at the eastern slopes of the Sredinny Range. Geological survey reports indicate that the faults are clearly visible in aerial and space images, as well as in geophysical data (gravimetric and anomalous magnetic fields) (Krykun et al., 2020). Faults in this zone are active, and their strike and normal sense (Zelenin and Garipova, 2022) are consistent with a model of transverse extension in Kamchatka due to slab rollback (Fig. 1).

In the study area, many of the faults are associated with chains of monogenetic edifices, indicating a relationship between faulting and magma-feeding systems formation, whereas others intersect cone edifices and lava flows with visible shifts along the fracture zones (Fig. 3a). There are three volcanic areas along the strike of the FZ, each exhibiting differences in geomorphology and the density of active faults (Fig. 2; Zelenin and Garipova, 2022). Near the SW slopes of the Chashakondzha volcano, the FZ intersects the Tigilsky Dol (TD, "Dol" is a Kamchatka toponym indicating a volcanic highland) monogenetic volcanic field. The TD is composed of numerous monogenetic centers (Fig. 3b) and small shield volcanoes, with chains of scoria and lava-scoria cones clustered along well-defined chains that mark the locations of magma-feeding fissures. Most of the fault scarps are buried below these volcanic landforms. Further to the SW, there is a Pliocene stratovolcano – Mount Oxi, after which this area is named (the Mount Oxi massif) (MO). In the study area, lava flows from numerous monogenetic scoria cones, small lava and shield volcanoes cover the western part of the massif up to 10–15 km from the main summit. Although this massif is highly eroded, fault scarps are clearly visible on the slopes of the valleys. The MO massif has the highest density of active faults within the entire SR. The Anaunsky Dol (AD), which is situated further to the SW, is a less eroded volcanic highland with numerous scoria and lava-scoria cones and several shield volcanoes, all within the studied fault zone. The highest summit of AD is the Anaun stratovolcano. The faults of AD produced long parallel scarps, surrounded by magma-feeding fissures with the same strike (Zelenin and Garipova, 2022).

This paper presents the findings of an investigation of a representative collection of 179 samples of volcanic rocks of varying ages that were erupted throughout the FZ (Fig. 2). We made a special effort to sample all structural levels, paying particular attention to the edifices that are spatially linked to the faults. In this work, we aim to better constrain the origins of the geochemical diversity in these monogenetic fields as a proxy for the generation of monogenetic fields generally and to explore the relationship between magmatism and tectonics.

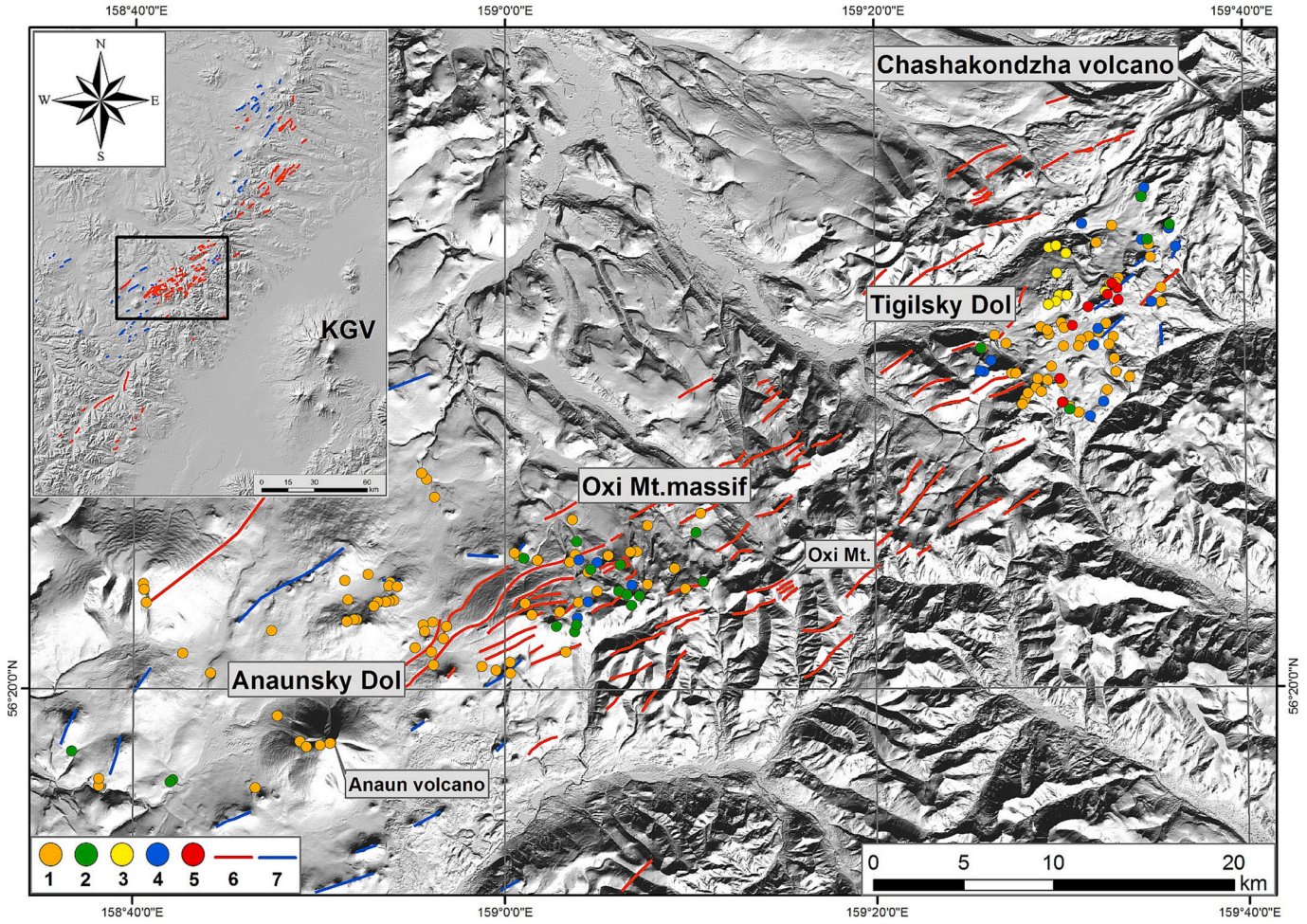

Fig. 2. A sample location map showing the distribution of active faults and magma feeding fissures in the study area and within the SR (inset) adapted from Zelenin and Garipova (2022). Legend: 1 – Group 1 medium-K rocks; 2 – Group 2 high-K rocks; 3 – Group 3 high-Ti basalts; 4 – Group 4 high-Mg basalts; 5 – Group 5 picrobasalts; 6 – active faults; 7 – magma feeding fissures. ArcticDEM data were used for the topographic base (Porter et al., 2018).

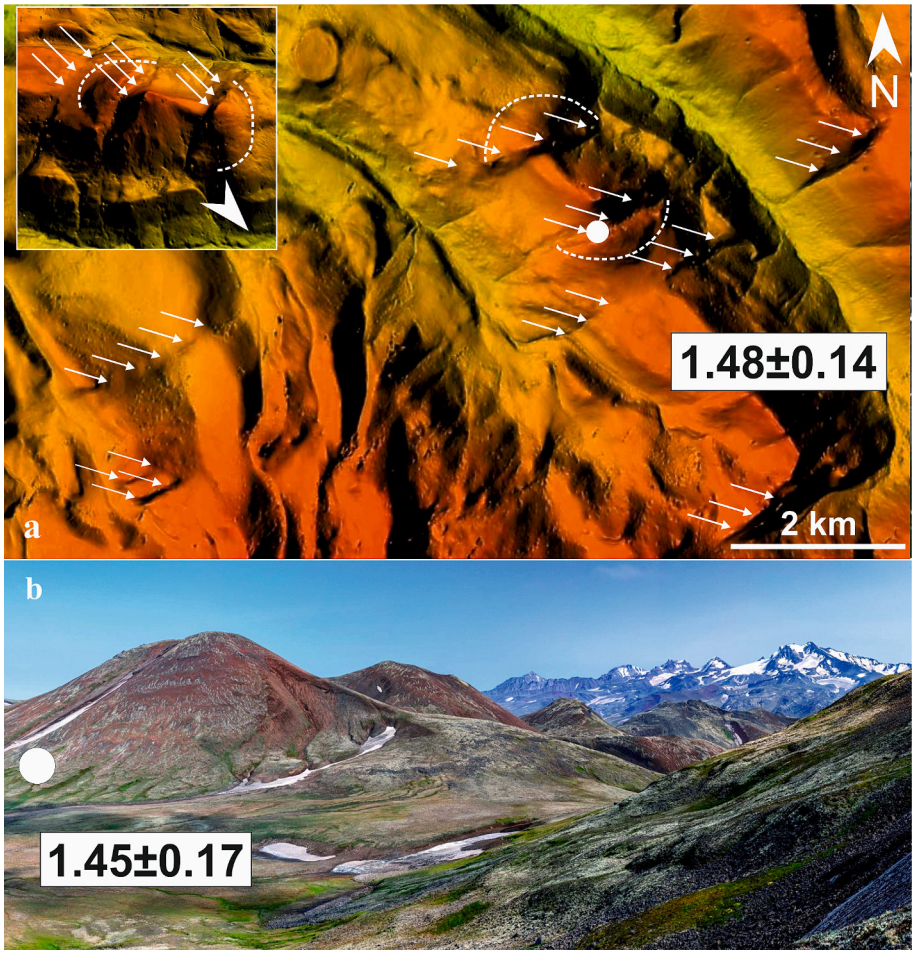

Fig. 3. (a) Subparallel faults near one of the Mount Oxi massif cones, outlined by arrows (ArcticDEM space image render). Based on field observations, the amplitude of the scarps (vertical displacement) reaches 7–8 m. Inset: A 3D model of the scoria cone. (b) A photograph of the Tigilsky Dol showing a chain of picrobasaltic scoria cones in the foreground and the Chashakondzha volcano in the background. Photo courtesy of Adam Kirilenko. The white dots shows the sampling sites for the K—Ar age determinations; the ages are shown on the image (Supplementary Material 1, Table S3).

3. Analytical methods

Major and trace element compositions of the sampled rocks together with those of the standards, are provided in Supplementary Material 1, Tables S1 and S2. The concentrations of major, minor and selected trace elements (V, Cr, Co, Ni, Cu, Zn, Rb, Sr, Y, Zr, Nb, Ba, Pb) were analyzed by X-ray fluorescence spectroscopy (XRF) using an Axios MAX vacuum sequential spectrometer (wavelength dispersive) (PANalytical) at the Institute of Geology of Ore Deposits, Petrography, Mineralogy, and Geochemistry RAS (IGEM RAS). Analytical errors were 1–5 rel% for the elements with concentrations >0.5 wt% and up to 12 rel% for the elements with concentrations <0.5 wt%. Additional trace elements were analyzed by inductively coupled plasma mass spectrometry (ICP-MS) using a mass spectrometer X-7 (Thermo Elemental, USA) at the Institute of Microelectronics, Technology, and High Purity Materials RAS (IMT RAS). The accuracy for most trace elements was ~7 rel%. Radiogenic argon analyses were conducted using the isotopic dilution method with ^{38}Ar as a tracer; the potassium content was determined by flame spectrophotometry using the MI-1201 IG mass-spectrometer complex at the IGEM RAS. The results are presented in Supplementary Material 1, Table S3.

Melt inclusions were homogenized using a batch approach with oxygen fugacity controlled at ambient pressure in a high-temperature gas-mixing vertical furnace Nabertherm® RHTV 1700 at the Vernadsky Institute of Geochemistry RAS. Analyses of glasses, Ol and Sp were acquired using the JEOL JXA-8230 electron microprobe at the Lomonosov Moscow State University. The precision (2σ) for Cl, S and F analyses in the glasses was ~5 rel%, ~2.5 rel% and ~ 15 rel%, respectively. The analytical precision (2σ) for minor elements in olivine was ~41 ppm for Ni, ~33 ppm for Mn, ~9 ppm for Ca, ~12 ppm for Al, ~19 ppm for Cr and ~ 8 ppm for Ti. Results of the analyses of samples and standards are presented in Supplementary Material 2, Tables S4–S7. The concentrations of the trace elements in the glasses of the melt inclusions in olivine were analyzed by secondary ion mass spectrometry. The results are presented in Supplementary Material 2, Table S8.

A detailed description of the analytical procedures, list of reference materials, standards used, analytical errors and detection limits can be found in Supplementary Material 3 (Appendix C).

4. Results

4.1. Ages of the main pulses of volcanic activity

Our K—Ar age determinations are presented in Supplementary Material 1, Table S3. The volcanic edifices of the FZ have been divided into two types based on their morphology: (1) plateau-like remnants of heavily eroded volcanoes; and (2) shield volcanoes, scoria cones and lava flows with relicts of the primary volcanic relief on their surface, including craters. The results of the K—Ar age determinations show that all rocks of the first type formed in the Pliocene (4.3–3.3 ± 0.14 Ma). Well-preserved volcanic centers began to form after 3.2 ± 0.11 Ma. Most eruptions at the TD MVF occurred in three stages: 1.5 ± 0.18 Ma, 1 ± 0.1 Ma, and from 0.3 ± 0.08 to <0.05 Ma. Similar stages of Quaternary volcanism can be distinguished within the MO. A set of K—Ar isotopic ages for the Anaunsky Dol volcanoes was published by Pevzner et al. (2020). Within the AD, there were at least two stages (3.2 ± 0.11 and 2 ± 0.14 Ma) of volcanic activity separated by a period of repose of about 1 Ma.

4.2. Whole rock geochemistry

All the rocks studied belong to the medium to high-K calc-alkaline series and are represented by a continuous evolutionary trend from picrobasalt to andesite (there are also a few samples of dacite and rhyolite), with basalts and basaltic andesites being the most prevalent (Fig. 5). The rhyolites are restricted to the eruptive activity of the Chashakondzha volcano, and the dacites represent a few domes that were extruded through the basement of the TD and MO. For the purpose of our discussion, we only consider rocks with basaltic and basaltic andesite composition, as the generation and evolution of high-Si rocks is beyond the scope of this paper. Most of the rocks that we studied are similar to the previously studied rocks of the SR (Volynets et al., 2010, 2018, 2020) with some exceptions (high-Mg basalts and high-LREE picrobasalts). On the basis of their major and trace element compositions, the rocks of the FZ can be divided into several groups.

The dominant rocks are ***medium-K lavas*** (Group 1, Fig. 4a, 5), ranging in composition from basalt to andesite, with moderate concentrations of MgO (<8 wt%, Mg# < 60) and TiO_2 (<1 wt%), that are similar to the rocks previously studied from the "eastern" flank of the SR (Volynets et al., 2018, 2020). Rocks of this group are found along the entire fault zone, and are of both Pliocene and Quaternary age.

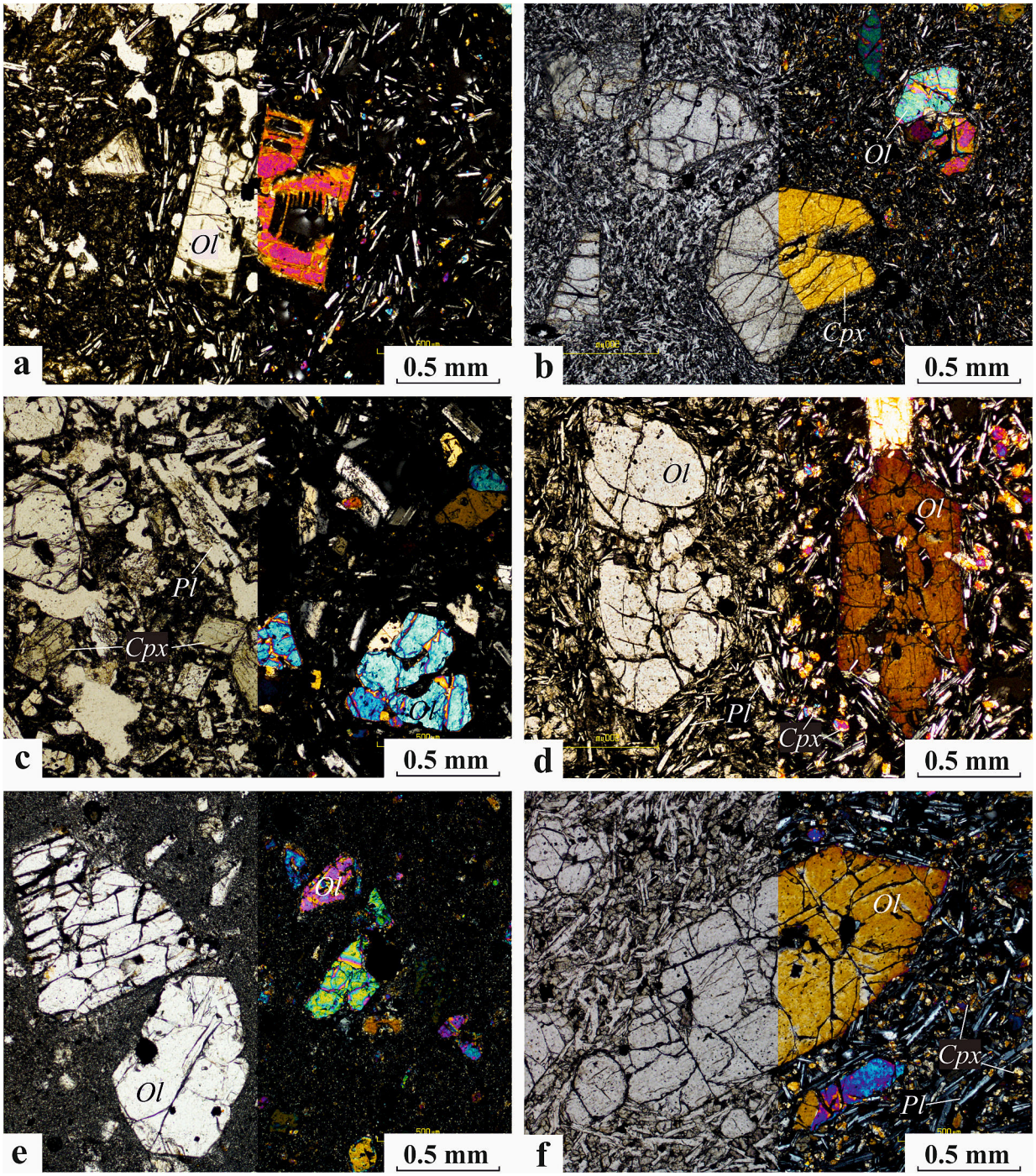

Fig. 4. Photomicrographs of the petrographic features of the studied rocks. (a) Group 1 (TIG-19-7876); (b) Group 2 (TIG-19-7861); (c) Group 3 (TIG-19-7827); (d) Group 4 (TIG-19-7732); (e) Group 4 (TIG-19-7734); (f) Group 5 (TIG-19-7874). The left and right sides of each photo are parallel and crossed polarized transmitted light images, respectively. Ol – olivine, Cpx – clinopyroxene, Pl – plagioclase.

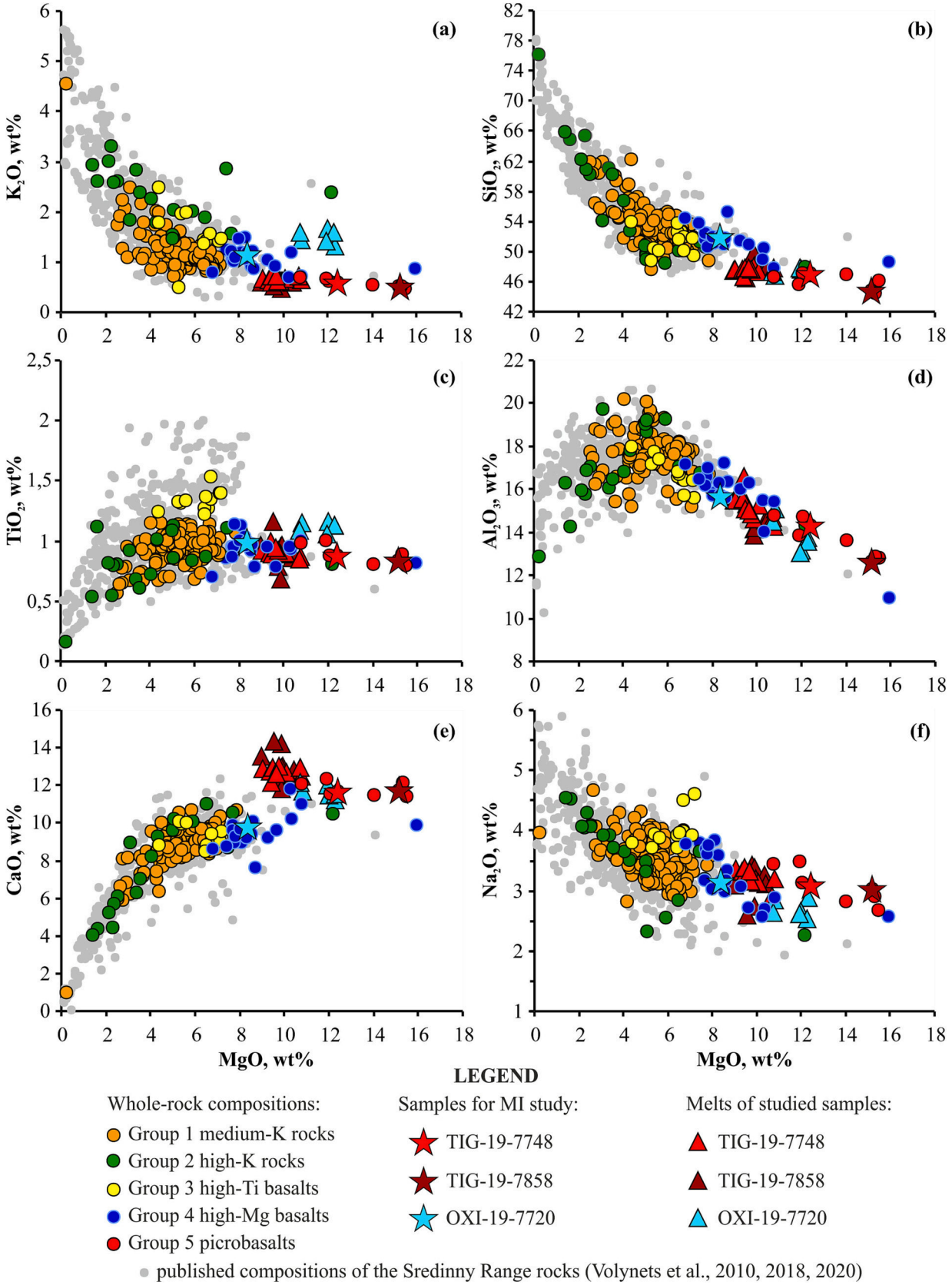

Fig. 5. Harker diagrams for whole rocks and melt inclusions.

Microscopically, the rocks are olivine-phyric with a hyalopilitic (Cpx-Ol-Pl-Mt) groundmass. Olivine phenocrysts up to 1 mm in diameter comprise ~5–7 vol% of the rock and frequently have a skeletal shape.

The medium-K rocks have arc-like geochemical signatures with high LILE/HFSE ratios and a prominent Nb—Ta anomaly (its depth varies in different samples, but Nb and Ta contents do not exceed 6 and 0.35 ppm, respectively) (Fig. 6a). The REE profiles are relatively flat, with a La/Yb ratio varying from 2.4 to 7.8 (it is 5.1 on average) (Fig. 7a). The $\Sigma REE_{average}$ value for basalts and basaltic andesites of Group 1 is 64 ppm and the ΣLREE (La to Sm) value is 51 ppm. The AD basalts and basaltic andesites have more variable REE concentrations. They are a little more enriched in LREE: the La/Yb ratio varies from 5.9 to 8.6 (it is 6.7 on average) and the $\Sigma REE_{average}$ is 78 ppm (ΣLREE ~64 ppm).

Rocks belonging to the ***high-K series*** (Group 2, Fig. 4b, 5), although not in great abundance, were found in all segments of the studied area. This group is formed almost entirely by basalts, andesites and dacites of the Pliocene basement (4–3.3 Ma), as well as by dacites and rhyolites of the Chashakondzha volcano; it also includes samples from a few young scoria cones (<50 Ka). Microscopically, the basic rocks of this group are Ol-Cpx-phyric with an intersertal groundmass (Cpx-Pl-Mt). They contain up to 5 vol% of phenocrysts, 0.5–1 mm in diameter; glomerocrysts of Cpx are frequent.

Compositionally, all the high-K lavas have an island-arc type of trace element distribution (Fig. 6b). Compared to Group 1, in addition to having higher potassium contents, they are slightly enriched in Rb, Sm, Eu and Gd, but the La/Yb ratio is almost the same (3.7–7.4) as is the $\Sigma REE_{average}$ value (Fig. 7b). There are three samples in this group with a Mg# >60, which were assigned to this group because of their high K_2O content. One of them (OXI-19-7724) differs from the others in the group by having substantially higher light and middle REEs concentrations; the La/Yb ratio is 12.5, ΣREE is 145 ppm with ΣLREE value of 123; the trace element profile has an island-arc signature, albeit with overall elevated REE concentrations. Another outlier is represented by the high-Mg high-K basalt from the AD with a Mg# 71 (AN-10-09): it has an elevated ΣREE content (91 ppm, with a ΣLREE content of 80 ppm) but a La/Yb ratio similar to that of the other rocks of this group (7.4).

High-Ti basalts (Group 3, Fig. 4c, 5) were found only within the TD, were formed during the last impulse of volcanic activity in this area (<50 Ka) and have built only one large effusive center. The rocks contain the assemblage Ol-Cpx-Pl-Mt (±Opx), are vesicular, serial-porphyric and have a hyalopilitic groundmass. The phenocrysts comprise about 5–10 vol% of the rock and are up to 1.5 mm in diameter; Cpx glomerocrysts are common.

Although they belong to the high-K series, these rocks differ from other high-K samples in their TiO_2 content; 1.2–1.53 wt% (Fig. 5c). Also, they are moderately enriched in all the incompatible elements compared to the other basalts of the fault zone, especially the HFSE (Fig. 6b). Their La/Yb ratio is 5.7–7.8 (Fig. 7c); the $\Sigma REE_{average}$ is 82 ppm, of which 68 ppm are ΣLREE. According to our previous studies, Quaternary high-Ti basalts are widely distributed in the northern and western segments of the SR, but normally they display a much higher enrichment in HFSE, than it is typical for the TD lavas (Volynets et al., 2010, 2018). For example, the Ta/Yb ratio is 0.12–0.17 in rocks from Group 3, whereas it can reach 0.5–0.6 in the high-Ti basalts from the Ichinsky, Kekuknaysky and Sedanka monogenetic lava fields (Fig. 8c); the Nb and Ta contents are 3.5–5.2 and 0.19–0.28 ppm, respectively, in the TD lavas but can be as high as 25.9 and 1.6 ppm, respectively, in the rocks from the above-cited locations.

High-Mg basalts (SiO_2 47.2–51.8 wt%) and high-Mg basaltic andesites (SiO_2 53.1–54.7 wt%) with MgO >8 wt% and/or a Mg# >60 are widely distributed within the TD and, to a lesser extent, within the MO (Group 4, Fig. 2, 4d, e, 5). They first appeared on the surface at the TD at 3.5 Ma. This was followed by a large pulse of high-Mg volcanism beginning at 1.5 Ma and, in turn, by periodic eruptions of high-Mg magmas at 1 Ma and 0.3 Ma.

The high-Mg basalts are olivine-phyric with an intersertal (Ol-Cpx-

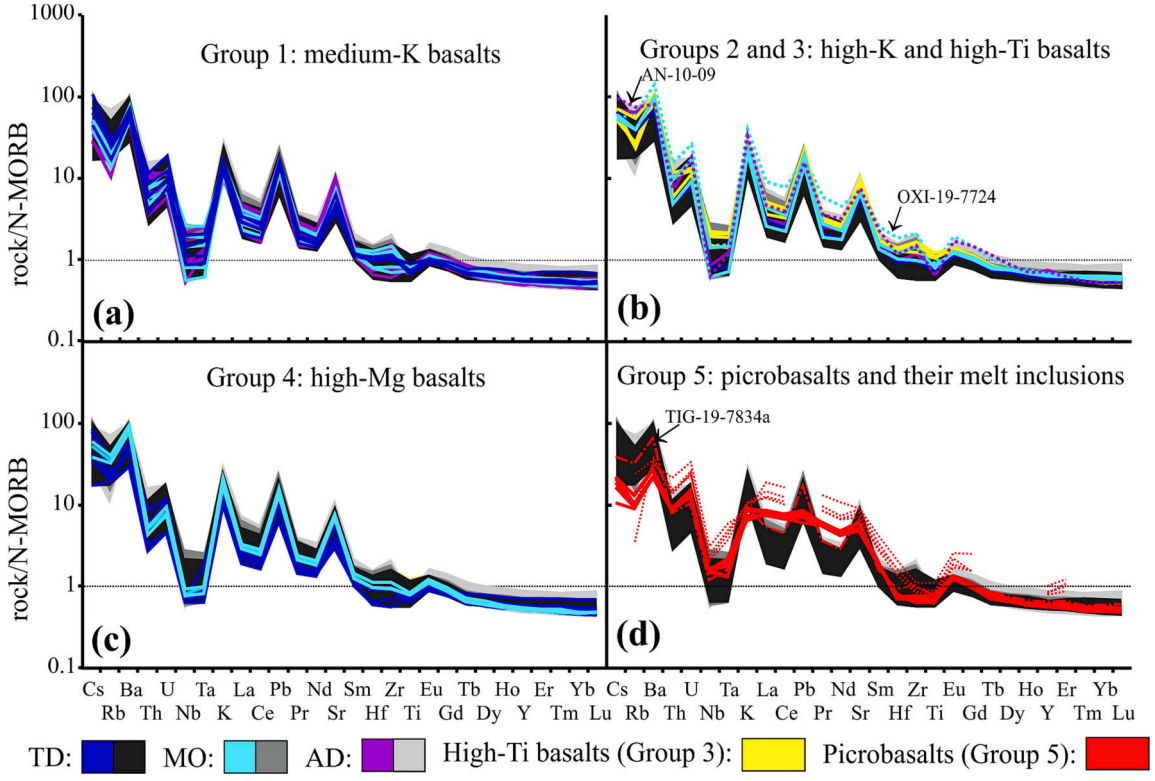

Fig. 6. N-MORB normalized trace element concentrations in the basaltic rocks of the study area. The samples discussed in the text are shown by dashed lines and denoted by a sample number. The thin dashed lines in (d) represent melt inclusion data. Black field, indicating TD compositions, doesn't include samples from Group 5, The N-MORB composition is from Sun and McDonough (1989).

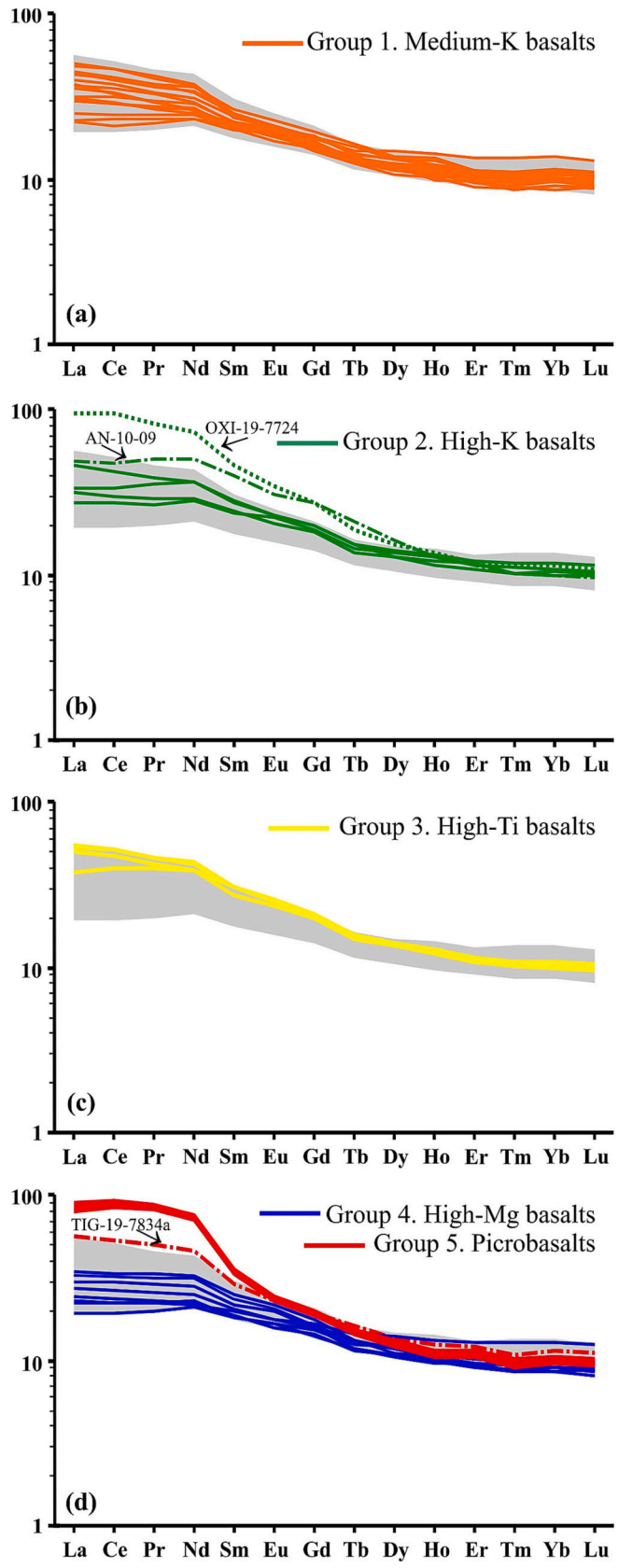

Fig. 7. Chondrite-normalized REE profiles for each of the rock groups. Grey field correspond to the compositions of samples from Groups 1–4 and does not include outliers (which are indicated by various dashed lines and denoted by a sample number) and samples from Group 5. The chondrite composition is from McDonough and Sun (1995).

Pl-Mt) or hyaline groundmass. Most of the phenocrysts are represented by idiomorphic or subidiomorphic olivine up to 2 mm in diameter, comprising 10–15 vol% of the rock, and sporadic Cpx glomerocrysts up to 1 mm in diameter. The olivine crystals in some samples show evidence of resorption.

From a geochemical standpoint, these rocks are similar to the medium-K series basalts (Group 1). They are characterized by moderate contents of TiO_2, an island-arc trace element signature with a deep Nb—Ta anomaly and are variably depleted in Zr and Hf (Fig. 6c). They have the flattest REE profiles of all the studied rocks (Fig. 7d), with a La/Yb ratio of ~4.4, an average ΣREE content of 59 ppm (with ΣLREE 40 ppm), and have the lowest concentrations of HFSE, Th and U of any of the rocks studied in this area. Within the AD area, only one lava flow was found with a high MgO content (Enkavtenup cone, sample AN-10-09). Unlike the other Mg-basalts, this lava flow also has a high K_2O content (2.35 wt%) and a different trace element distribution (i.e., higher LILE, Hf, Zr, light and middle REE concentrations than the other Mg-basalts) (Fig. 7b). For this reason, it was assigned to Group 2 (high-K rocks).

Picrobasalts (SiO_2 43.9–46.5, MgO 11.7–15.2 wt%, Group 5, Fig. 4f, 5) found within the TD are the most unusual volcanic rocks not only associated with this fault zone but also for the whole of Kamchatka. According to our age determinations, their eruptions took place at about 1.5 Ma. These rocks are strongly porphyritic with an intersertal (Cpx-Pl-Mt) groundmass and contain up to 20–25 vol% of idiomorphic olivine phenocrysts, some of which show slight traces of resorption.

Previously, high-Mg rocks in Kamchatka were documented mainly for Quaternary eruptions of several CKD volcanoes (Portnyagin et al., 2007 and references therein), and were found sporadically at several localities in the EVF: Avachinsky volcano (so-called avachites: Kepezhinskas et al., 1997; Volynets, 1994), at Gorely volcano (Duggen et al., 2007), on the Mt. Medvezh'ya cone near Koryaksky volcano (Nekrylov et al., 2022) and cones in the Azhabachye lake area (Nishizawa et al., 2017)). Within the SR, high-Mg rocks have been found as isolated scoria cones or lava flows (for example, the Enkavtenup cone in the AD; Volynets et al., 2010, 2018, 2020), but they have never been documented in such a large area or in the chains that we discovered in the TD (Fig. 2). All of the above mentioned Kamchatka high-Mg rocks have a high silica content (>49 wt%), whereas the rocks that we discovered in the TD have a picrobasaltic composition (SiO_2 > 43.9 wt%). Rocks with such low silica contents have never been described previously for the Quaternary volcanism of Kamchatka. The picrobasalts also generally have a lower K content, and higher contents of Al, Ca and Mn than the CKD high-Mg basalts. The concentrations of Cr (up to 1372 ppm) and Ni (up to 432 ppm) in the picrobasalts with MgO > 14 wt% are higher than those in CKD rocks and are close to those of avachites, although the latter have lower alkali contents and a higher silica content. Compared to the Group 4 high-Mg basalts, they are enriched in Ca, Cr, Co, Ni, Cu and Li and depleted in K, Cs, Rb, Ba and Zr.

The unique characteristics of the TD picrobasalts are not limited to the unusually high concentrations of magnesium. These rocks also have extremely high LREE concentrations for subduction-derived Kamchatka volcanic rocks: 20 ppm La, 54 ppm Ce, 8 ppm Pr, 34 ppm Nd on average, which exceed those of high-Mg basalts (group 4) by 3–4 times (Fig. 6d, 7d). Their total REE content varies from 130 to 141 ppm, with the LREE constituting 117–127 ppm. The Ce/Pb, K/La, Ba/Th, Ba/La and Sr/Nd ratios of the picrobasalts are close to mantle values, unlike the rest of the SR rocks, which show typical island-arc characteristics (Fig. 8). At the same time, the HFSE and HREE concentrations in the Group 5 rocks are low, close to N-MORB and lower. The N-MORB-normalized trace element profiles for this group have an exotic look, differing significantly from those of island-arc and ocean ridge settings. Their profiles are typical for the SSZ with Ba and U maxima, Nb—Ta and Hf-Zr-Ti minima, but demonstrate an absence of maxima for K, Sr and Pb, although not because of the low concentrations of these elements, but rather due to the extremely high content of REE (Fig. 6d). Only one sample of picrobasalt (TIG-19-7834a) exhibits transitional features,

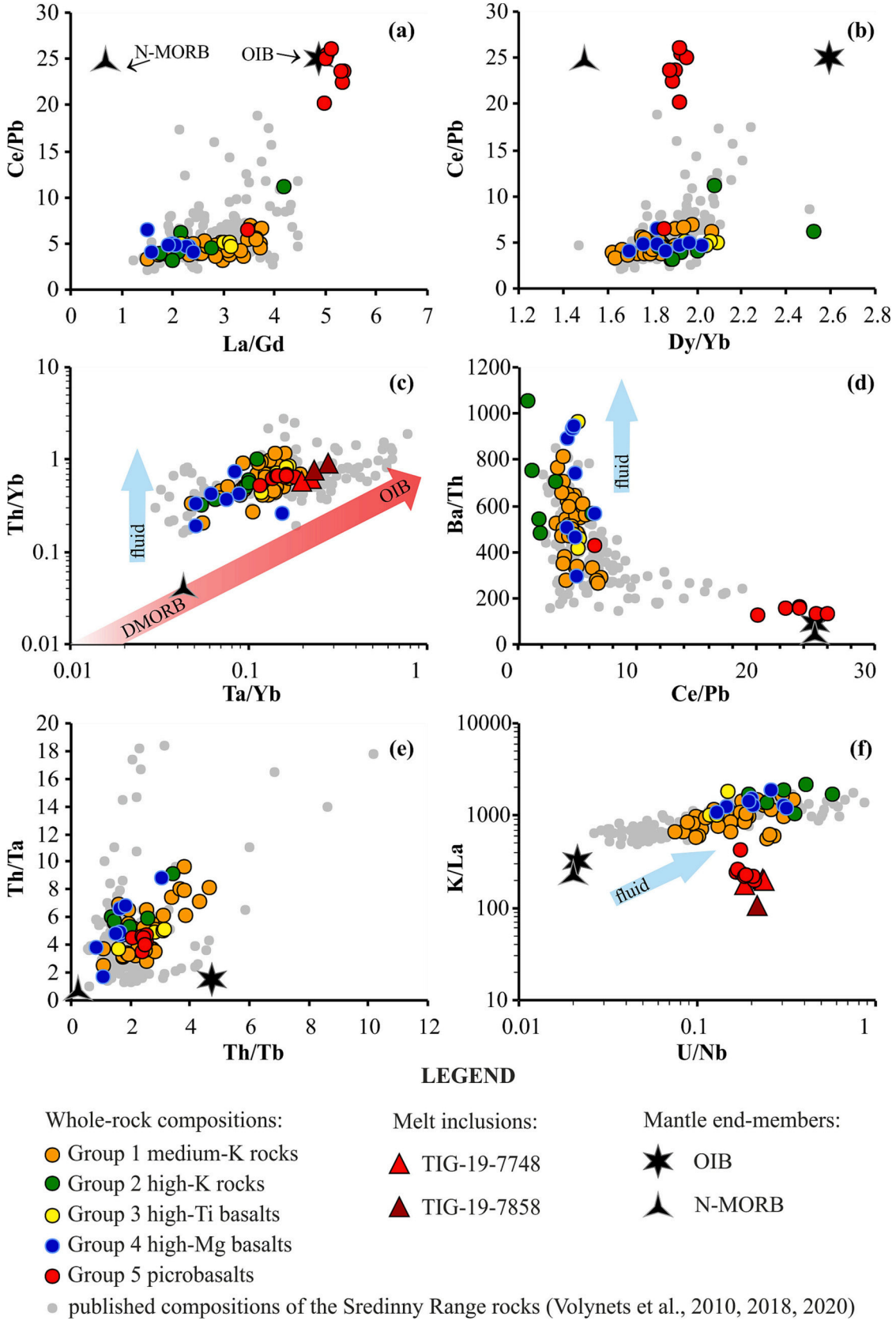

Fig. 8. Binary plots of incompatible element ratios for bulk rock and melt inclusion samples. The composition of the mantle end-members is from Sun and McDonough (1989).

namely an enrichment in the LREE (although not as strong as for the rest of the group; Fig. 7d) together with all the characteristics typical of subduction, including K, Pb, Sr maxima. Owing to this unusual feature of the Group 5 rocks, we refer to them hereafter as ***high-LREE picrobasalts***.

We made a preliminary analysis of the area covered by lavas of the different groups. Group 1 lavas occupy about 87% of the area, Group 2 and 4, about 3% each, Group 3 about 6% and Group 5 occupies <1% of the area.

4.3. Mineralogy and melt inclusions data

Ten samples were selected for detailed mineralogical study (olivine and spinel) on the basis of their chemical composition: Group 2 (high-K basalts) – OXI-19-7724, Group 3 (high-Ti basalts) – TIG-19-7827, Group 4 (high-Mg basalts) – 4 samples: TIG-19-7734, TIG-19-7870, OXI-19-7720 and OXI-19-7807, and Group 5 (high-LREE picrobasalts) – 4 samples: TIG-19-7746, TIG-19-7748, TIG-19-7874 and TIG-19-7858. The compositions of the minerals are provided in Supplementary Material 2, Tables S5 (olivine) and S6 (spinel).

4.3.1. Olivine

The measured olivine Mg# (Mg/(Mg + Fe)*100, mol%) in the above samples ranges from 79.3 to 93.2 mol% (Fig. 9). The least Mg-rich olivine crystal was in the high-Mg sample TIG-19-7734 and the most Mg-rich crystal in the high-Mg sample OXI-19-7807. Olivine with a Mg# exceeding 93 mol% is known only from Cretaceous picrites in Kamchatka (Kutyrev et al., 2021) and has never been reported for Quaternary magmatic rocks. The previous "record" belongs to olivine from the high Mg-basalts of the Shiveluch and Kharchinsky volcanoes – 92.6 mol % (Gorbach et al., 2023; Gorbach and Portnyagin, 2011).

The NiO content of the olivine from Group 5 (up to 0.4 wt% at a Mg# of 92.5 mol%) is typical of MORB olivine (Fig. 8a). Olivine from all the other samples contains an average ~ 0.1 wt% enrichment in this component relative to olivine from MORB with the same Mg#. Some olivine crystals from high-Mg sample OXI-19-7720 have NiO content as high as 0.5 wt%, which within Kamchatka is comparable only to that of

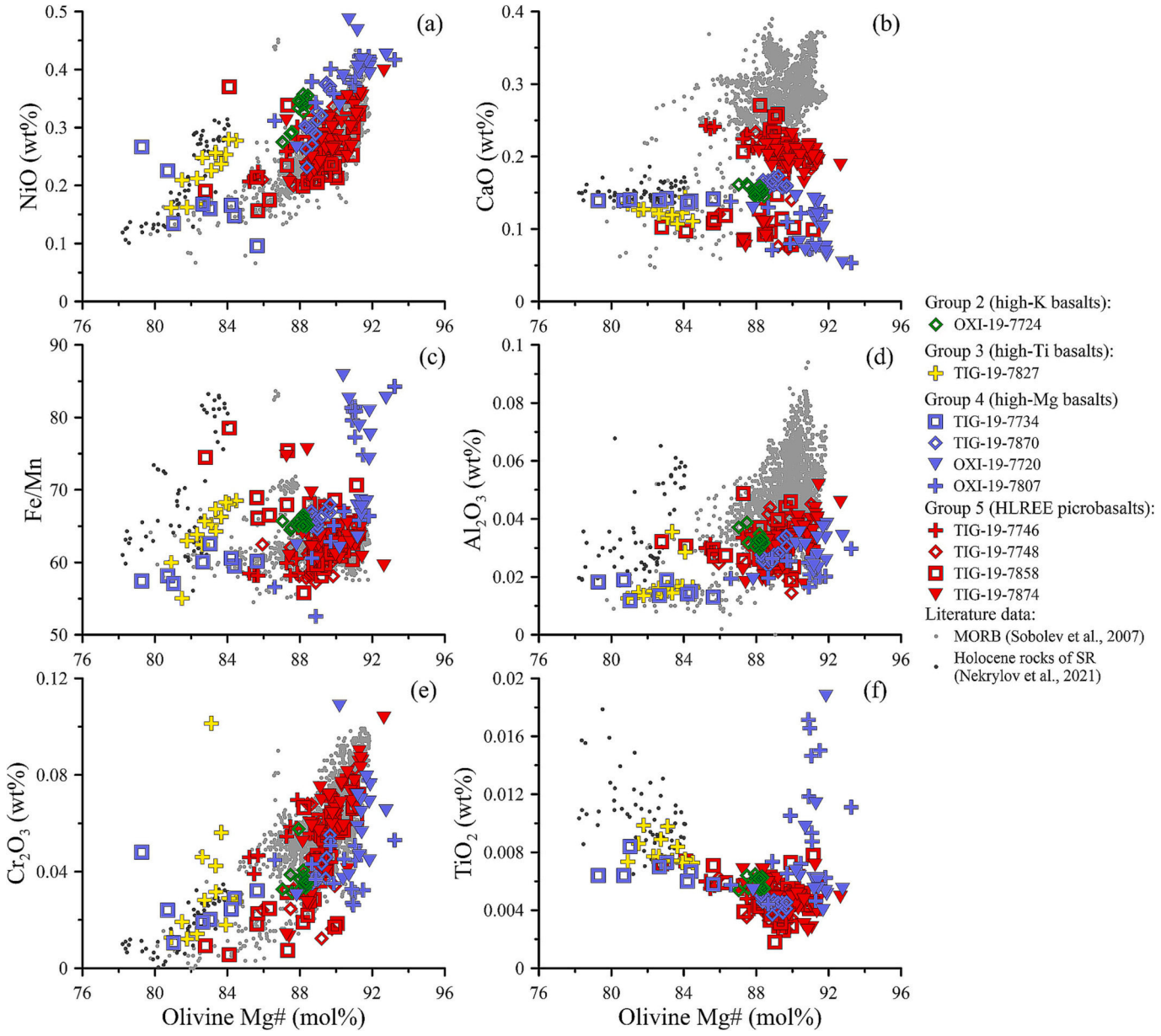

Fig. 9. Binary plots of minor elements contents versus the olivine phenocryst Mg#. The MORB data of Sobolev et al. (2007) and previously published data for the Late Quaternary SR basalts (Nekrylov et al., 2021) are shown for comparison.

some samples from the Kharchinsky volcano and a volcanic field near Lake Azhabachye (Gorbach et al., 2023; Nishizawa et al., 2017).

The CaO content of the olivine varies widely; however, it is lower than typical MORB values for all the samples (Fig. 9b). Olivine from Group 5 has the highest (and closest to MORB) CaO content, however, some of the crystals fall in the low-Ca group. The low-Ca group generally comprises basalts of the MO and high-Ti samples from the TD (OXI-19-7720, OXI-19-7807 and TIG-19-7827). Olivine from samples OXI-19-7724 and TIG-19-7870 has a composition intermediate between those of the low- and high-Ca groups.

The Fe/Mn values for olivine from most of the samples are in the 60–70 range (Fig. 9c). Only olivine from Mg-rich basalts of the MO and some olivine crystals of high-LREE picrobasalts have elevated values, up to 85.

The Al_2O_3 and Cr_2O_3 contents of the olivine differ among the samples, but not as strongly as for other components (Fig. 9d, e). Olivine from Mg-rich basalts of the MO have slightly lower contents of these components than olivine with the same Mg# from other samples. The Ti in olivine displays the opposite trend; the majority of the olivine crystals from the Mg-rich basalts of the MO are strongly enriched in Ti relative to olivine from other samples.

4.3.2. Spinel

The Cr# (Cr/(Cr + Al) × 100, mol%) of the olivine-hosted spinel inclusions varies widely from 36 to 81 mol% (Fig. 10a), although the variation within samples is quite small ~4 mol%. Spinel in the high-K basalt of the MO has the lowest Cr# (40.1 ± 4 mol%), the Mg-rich basalts of the MO have the highest Cr# (76.6 ± 3.7 for OXI-19-7807) and high-LREE picrobasalts of the TD have intermediate Cr#s (from 45 to 65 mol%). Values of Cr#s as high as 70–80 are typical for spinel from the CKD volcanoes (Nekrylov et al., 2018a), but it is the first description in the SR rocks to our knowledge.

The calculated Fe^{2+}/Fe^{3+} ratios for the spinel also vary widely, but in the range typical of Kamchatka spinel (Fig. 10b). Spinel from Mg-rich basalts of the MO and sample TIG-19-7858 have the lowest Fe^{2+}/Fe^{3+} ratio for the given Mg# of the host-olivine (from 0.7 to ~2 for olivine with a Mg# of 92), whereas spinel from TIG-19-7870 has the highest ratio (up to 3.5 for olivine with a Mg# of 90).

4.3.3. Olivine-hosted melt inclusions

Melt inclusions were studied in two samples from Group 5, TIG-19-7748 and TIG-19-7858, and one sample from Group 4, OXI-19-7720. The reheated melt inclusions have round shapes and contain homogeneous glass, gas bubbles and spinel crystals. The composition of the glasses from Group 5 samples falls within a narrow range, corresponding to that of medium-K basalt (Supplementary Material 2, Table S7), whereas the glasses from melt inclusions in OXI-19-7720 are high-K basalts. The glasses are depleted significantly in FeO and MgO and enriched in components that are incompatible with olivine. This is attributed to post-entrapment modifications of the melt inclusions. The Cl and F contents of the glasses of Group 5 samples are almost invariant, with Cl at approximately 0.03 wt%, F at ~0.1 wt% and SO_3 up to 0.3 wt % (Fig. 10). The melt inclusion glasses of OXI-19-7720 have considerably higher contents of Cl (~0.09 wt%) and SO_3 (up to 1.24 wt%) than the Group 5 melt inclusion glasses but nearly the same content of F (~0.11 wt%) (Fig. 11).

Trace element concentrations were measured by ion microprobe in melt inclusions but only for samples from Group 5 (inclusions in OXI-19-7720 are smaller than the analytical method allows) (Supplementary Material 2, Table S8). These concentrations yield profiles of incompatible element distribution that are similar to those of the corresponding rocks, but the absolute concentrations are higher for all elements measured except Rb (Fig. 6d). The LREE content (La up to 46, Ce – 120, Pr – 17, Nd – 76, ΣLREE 167–269 ppm) is exceptionally high but the La/Yb ratios from 10.8 to 16.8 preserve the shape of REE distribution profiles of their host rocks.

4.3.4. Temperature and oxygen fugacity

The crystallization temperature and oxygen fugacity of the magmas were estimated from the composition of olivine-spinel pairs using the models of Coogan et al. (2014) and Ballhaus et al. (1991), respectively. These models have their limitations with respect to the FeOt of the spinel (< ~25–30 wt%; Ballhaus et al., 1991) and Fe^{3+} ($0.15 > Fe^{3+}/(Fe^{3+} + Cr + Al)$; Coogan et al., 2014). Consequently, it was not possible to reliably estimate temperature and oxygen fugacity for samples TIG-19-7827 and TIG-19-7734. The temperatures estimated for the crystallization of the olivine-spinel pairs vary widely and can show a range of up to 100 °C for a given olivine Mg# (Fig. 12b). However, on average, the temperature decreases from ~1270 °C at an olivine Mg# of 92.7 mol% to 1140 °C for an olivine Mg# 87.6 mol%. In contrast, the estimated oxygen fugacity is quite uniform (Fig. 12a). The least oxidized sample is the high-Mg basalt of the TD with a ΔQFM value of +1 ± 0.35 log. units and the most oxidized are the high-Mg basalts of the MO with ΔQFM values up to +2 log. units.

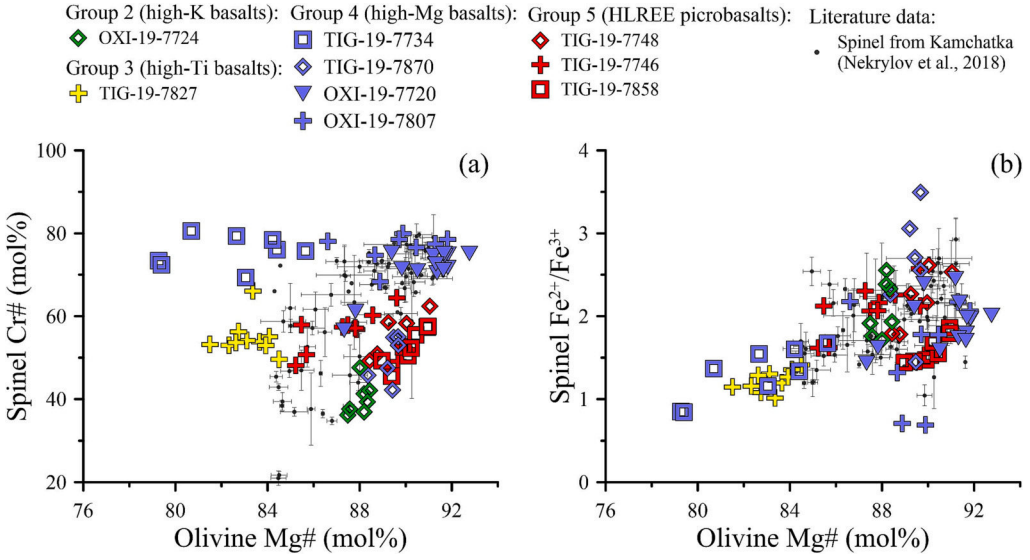

Fig. 10. Plots of spinel Cr# versus olivine Mg# for the various Sredinny Range rock groups. Also shown are the previously published compositions of spinel from Kamchatka basalts (Nekrylov et al., 2018a).

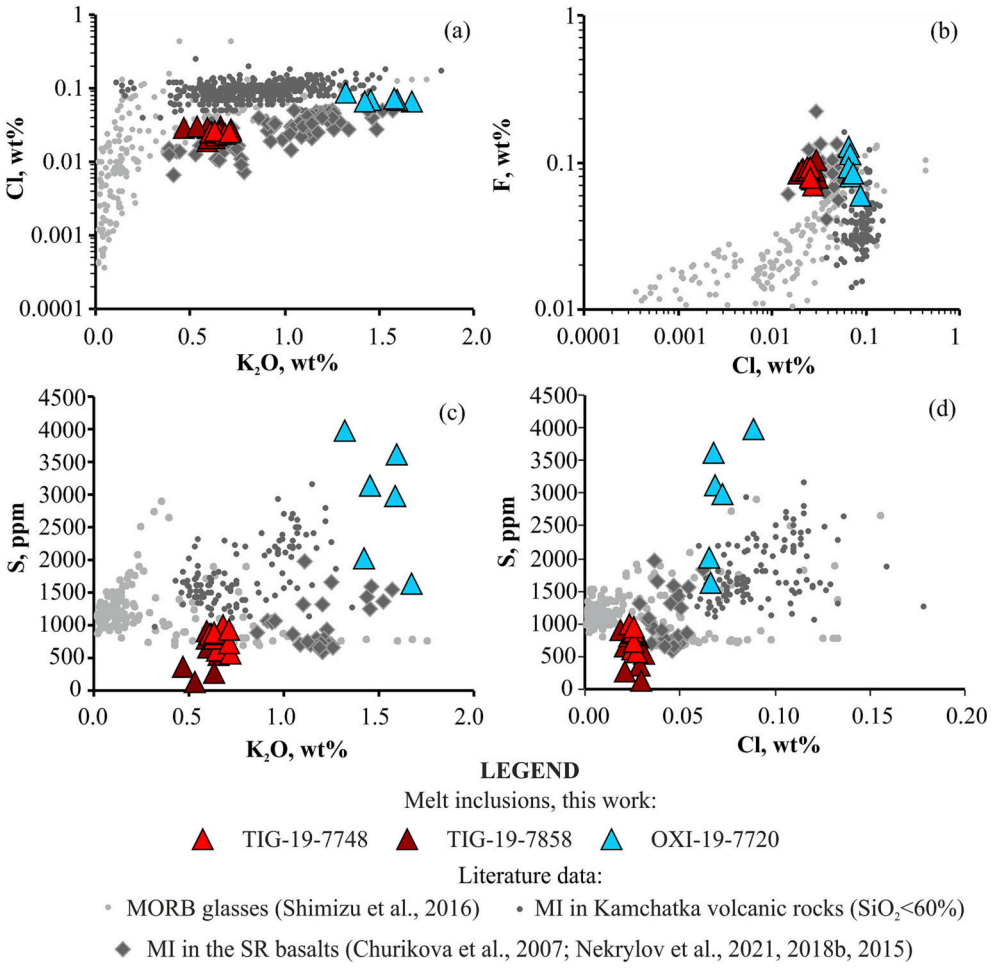

Fig. 11. The volatile content of melt inclusions from three samples collected in the study area. Also shown are corresponding melt inclusion data for MORB (Shimizu et al., 2016) and Kamchatka volcanic rocks downloaded from the GEOROC database (https://georoc.eu/) on 29 August 2022, using the following parameters: geological setting– Continental Margin: Kamchatka arc and sample criteria – melt inclusion; detailed references to the data sources can be found in Supplementary Material 4 (Appendix D).

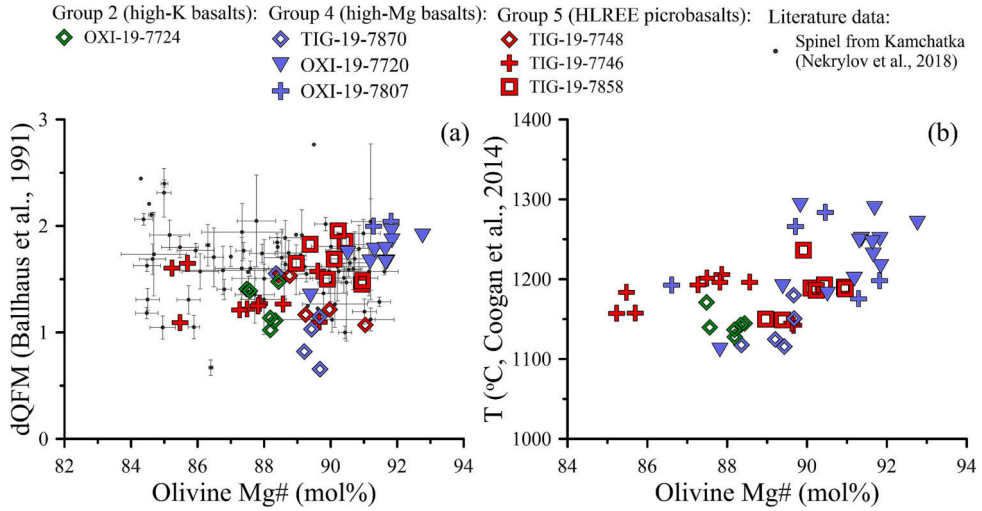

Fig. 12. Oxygen fugacity versus crystallization temperature calculated using the olivine-spinel oxygen barometer and geothermometer, respectively. See main text for more detail.

4.3.5. Reconstruction of melt composition

The melt inclusions show a significant deficiency in FeO relative to the composition of the related lavas, and lavas from the same volcanic field with the same MgO content. This loss of FeO is a common phenomenon for olivine-hosted melt inclusions and is not considered to reflect negatively on the quality of the analyses of the other components (Danyushevsky et al., 2000). The most reliable way to estimate the initial FeO content of the melt is from the composition of the related rocks. The bulk-rock Mg# of both the high-LREE samples is significantly higher than required for equilibrium with the olivine in them, and reflects their cumulate nature. We estimated the initial FeO content of the melt by subtracting the average composition of the olivine in each

sample from the bulk rock composition until an equilibrium composition was achieved. These calculations yielded 9.4 wt% FeO for the olivine in sample TIG-19-7748 and 10.9 wt% FeO for that in sample TIG-19-7858. Such a large difference in the initial FeO content of melt inclusions from samples of very similar composition is unlikely and should be reflected in a large difference in the melt crystallization temperature. However, the olivine-spinel geothermometer returned a temperature of 1202 ± 37 °C for sample TIG-19-7748 (for an olivine Mg# of 89.6 ± 1 mol%) and 1185 ± 27 °C for sample TIG-19-7858 (for an olivine Mg# of 90.1 ± 0.7 mol%). Consequently, it is safe to assume that the temperature difference between these samples was insignificant and that at least one of the estimates of the initial FeO content of the melt is incorrect. In contrast to the two samples discussed above, the bulk rock Mg# of sample OXI-19-7720 is lower than required for equilibrium with the olivine hosting the melt inclusions. The initial FeO content for this sample was estimated to have been 8.5 wt% by reversing the olivine crystallization for the whole-rock composition until equilibrium with the average composition of the olivine was reached. This was done using the Petrolog3 software (Danyushevsky and Plechov, 2011). The crystallization temperature estimated for sample OXI-19-7720 is nearly the same as that estimated for the high-REE samples, 1221 ± 56 °C (for olivine with a Mg# of 90.7 ± 1.6 mol%).

Another phenomenon that may affect melt inclusion composition is the loss of water after entrapment (e.g. Portnyagin et al., 2008). In addition to causing the initial water content of the melt to be underestimated, it can also have a significant impact on the SiO_2 content, as demonstrated by Portnyagin et al. (2019). The melt inclusions in all the samples have nearly the same SiO_2-saturation index (Qz*, Portnyagin et al., 2019), i.e., 0 ± 0.022 for TIG-19-7748, 0.026 ± 0.035 for TIG-19-7858 and − 0.03 ± 0.024 for OXI-19-7720. However, the SiO_2-saturation indices of their host rocks vary considerably (0.074, −0.006 and 0.21, respectively). As the bulk rock compositions of samples TIG-19-7858 and OXI-19-7720 could have been affected significantly by mineral accumulation and assimilation during fractional crystallization, particularly in respect to FeO and SiO_2, we chose the composition of sample TIG-19-7748 as a reference for correcting the melt inclusions in all the other samples.

We employed the Petrolog3 algorithm of Danyushevsky and Plechov (2011) to reconstruct the original compositions of the trapped melts and used it to equilibrate the compositions of the melt inclusions with those of their olivine host for the reference FeOt concentration of 9.4 wt% (sample TIG-19-7748). The oxygen fugacity used in the calculations was set to ΔQFM +1.3 log. units for TIG-19-7748 and ΔQFM +1.7 for TIG-19-7858 and OXI-19-7720 based on olivine-spinel estimations. The pressure was assumed to be 0.1 MPa. We used the model of Ford et al. (1983) for olivine-melt equilibration and that of Borisov and Shapkin (1990) for the dependence of the Fe^{3+}/Fe^{2+} ratio on the redox conditions of the melt. To calculate the concentrations of S, Cl, F and H_2O in the reconstructed melts, we corrected the measured concentrations for the volume of olivine that was added to the melt inclusions during our modeling. The compositions of the reconstructed melts are provided in Supplementary Material 2, Table S7.

5. Discussion

The nature of the voluminous monogenetic volcanism in the Sredinny Range is the subject of ongoing debate, and remains poorly understood because of the remoteness of the region. Over the past few decades, however, there have been a series of publications dedicated to this issue. For example, Churikova et al. (2001) reported on the compositions of numerous scoria cones and lava flows surrounding the Ichinsky stratovolcano, suggesting that the magmas formed through fluid-induced melting of a mantle source enriched to varying degrees in HFSE. Volynets et al. (2010, 2018, 2020) conducted a regional investigation of the SR volcanism, involving MVFs from virtually all parts of the Range. Their results suggest that the SR has a complex geological history, involving a heterogeneous mantle source in some parts and an enriched mantle source in the western and northern parts. Quaternary rocks from the eastern and central flanks of the southern part of the SR, including those of both monogenetic and stratovolcano origin, exhibit well-defined island-arc signatures, only slightly enriched in HFSE. Nekrylov et al. (2015, 2018b, 2021) reported on the compositions of melt inclusions in olivine from the Late Quaternary eruptions of the Kekuknaysky, Sedanka, Tobeltsen and Ichinsky MVFs, arguing that their enriched compositions may have been produced by partial melting of a variety of delaminating lower crustal lithologies containing pyroxene and amphibole, as well as the surrounding peridotites. In this section, we use the geochemical and mineralogical data presented earlier to explain the phenomena observed in the study area within the broader regional tectonic context.

5.1. Diversity of the volcanic rocks compositions within the fault zone

Although the volcanic rocks of the FZ are unusual in several ways, their most conspicuous feature is their exceptional compositional diversity. Kamchatka hosts numerous monogenetic volcanic fields, but in most cases, the compositions of the volcanic rocks within each zone belong to the same group. In the Sredinny Range, for example, the Sedanka and Kekuknaysky MVFs produced tens of scoria cones and lava flows, as well as small shield volcanoes, all of which have very similar compositions corresponding to those of high-Ti HFSE-enriched basalts and basaltic andesites (Koloskov et al., 2013; Volynets et al., 2010). The Ichinsky MVF hosts two types of volcanic rocks, high-Ti HFSE-enriched basalts compositionally transitional between within-plate and island-arc types, and medium-K medium-Ti basalts of the island-arc type (Churikova et al., 2001). Tolbachinsky Dol in the CKD is well-known for its occurrences of high-Mg and high-Al types of basalt in the same district (Churikova et al., 2015; Portnyagin et al., 2015).

Within the TD, we found five varieties of volcanic rocks, ranging in composition from medium-K medium-Ti, high-K, high-Ti and high-Mg basalts to picrobasalts. In many cases rocks of different composition occur in neighboring scoria cones, sitting on different faults. Although all the volcanic rocks of the FZ demonstrate island-arc affinity (variably low HFSE content, elevated LILE and LILE/HFSE ratios), it would be difficult to explain the ranges in their compositions by fractionation from a single source. The trace elements ratios require the involvement of different magma batches from heterogeneous sources, which vary in fluid composition and volume. Nevertheless, it is interesting to note that the trace element distribution in the high-Mg basalts (Group 4) is very similar to that of the high-Mg basalts of the Klyuchevskoy volcano (Churikova et al., 2001). This volcano is situated closer to the trench at the same latitude as the SZ, implying a similarity in mantle composition that is characterized by local small-scale heterogeneity.

5.2. Volatile components of the magma

The main volatile components of the SSZ melts are H_2O, CO_2, S, Cl and F (e.g., Fischer, 2008) and there are a lot of complications in estimations of their initial contents for ancient rocks. We have estimated the contents of Cl, F, S and H_2O (in descending order of reliability) for the reconstructed magmas that produced the TD and MO lavas.

Chlorine and fluorine. The Cl contents of the melts are 0.025 ± 0.001 wt% for TIG-19-7748, 0.025 ± 0.005 wt% for TIG-19-7858 and 0.072 ± 0.009 wt% for OXI-19-7720. It is noteworthy that, despite generally low Cl contents, the melts of the MO contain nearly three times more Cl than the melts of the TD. In contrast, the F contents of the three samples are indistinguishable within the margin of error: 0.084 ± 0.008 wt%, 0.089 ± 0.008 wt% and 0.093 ± 0.025 wt%, respectively.

Sulfur. Precise estimation of the S content of melts is complicated by its post-entrapment behavior. Firstly, S is highly volatile and a significant part of it can be easily redistributed into the shrinkage bubble of melt inclusions (e.g., Venugopal et al., 2020) or escape the melt

inclusion via unnoticed cracks in the host olivine. Secondly, sulfur tends to form a sulfide phase in the glasses of olivine-hosted melt inclusions during Fe-loss (Danyushevsky et al., 2000). However, a significant redistribution of S to shrinkage bubbles has only been demonstrated for water-rich melt inclusions, and has not been observed for dry melt inclusions (Korneeva et al., 2023). Furthermore, there was no evidence of daughter sulfide phases in the melt inclusions, but we still cannot exclude the possibility that a portion of the S was trapped in shrinkage bubbles or escaped through undetected fractures in the olivine. Thus, we can discuss only the highest estimated contents of S in the melt inclusion glasses. These contents are 0.1 wt% for TIG-19-7748, 0.091 wt% for TIG-19-7858 and 0.4 wt% for OXI-19-7720. The 0.1 wt% S estimated for high-LREE picrobasalts is quite low for melts at such a high oxidation state (above QFM + 1, Fig. 11), which may indicate strong undersaturation of their source in S. It is worth noting that the low SO_3 content in the melts of high-LREE picrobasalts is accompanied by their enrichment in Cu, up to 170 ppm in non-cumulate samples versus 90 ± 30 ppm in the other rock-types investigated. This can be explained by the total dissolution of sulfides in the source during melting. Such magmas, enriched in chalcophile elements and depleted in S in post-subduction settings, could originate from second-stage melting of the subduction-modified lithosphere (e.g., Richards, 2009). It should also be noted that the 0.4 wt% S estimated for the OXI-19-7720 melt is at the upper end of the range of S contents of SZ melts (Zelenski et al., 2022).

Water. The estimates of the H_2O content of the melts are the least reliable of the estimates of the volatile components referred to above. The problem is that the initial water content is never preserved in olivine-hosted melt inclusions from slowly cooled samples of lava or even volcanic bombs (Lloyd et al., 2013). However, we know that the melts investigated contained a significant amount of water for the following reasons: 1) geochemical markers for H_2O-rich fluids such as high-LILE and low HFSE contents are observed; 2) the CaO content of the olivine is low, indicating high H_2O activity in the melt (Gavrilenko et al., 2016); 3) there is a strong SiO_2 deficiency in our melt inclusions relative to the composition of the related lavas (Portnyagin et al., 2019). The H_2O content was estimated from the model of Gavrilenko et al. (2016) which yielded a value of 2.6 ± 0.4 wt% for TIG-19-7748, 2.2 ± 1 wt% for TIG-19-7858 and 5.5 ± 1 wt% for OXI-19-7720. Use of this model, however, can lead to an overestimation of the H_2O content, which has been the case for other samples from the Sredinny Range (Nekrylov et al., 2018b). The model of Portnyagin et al. (2019), however, allows the H_2O content to be calculated and the melt inclusion composition to be corrected for any deficiency in SiO_2. If we assume the $\Delta H_2O/\Delta SiO_2$ to be 1, this model predicts water contents of 1.49 ± 0.44 wt% for TIG-19-7748, 1.24 ± 0.21 wt% for TIG-19-7858 and 1.93 ± 0.38 wt% for OXI-19-7720. Nonetheless, as the $\Delta H_2O/\Delta SiO_2$ ratio may vary from 0.5 to 2, it is possible to over- and under-estimate the original water content in the melt by a factor of up to two. Estimates based on the two models show that the high Mg basalts from the MO contained more H_2O than the high-LREE picrobasalts of the TD.

An alternative approach to estimating the H_2O content of melts is by comparing the results obtained from independent geothermometers (e.g., Sobolev et al., 2016). In our case, we used geothermometers based on olivine-spinel (Coogan et al., 2014) and olivine-melt (Almeev et al., 2007; Ford et al., 1983) equilibria. By fitting the olivine-melt temperatures to those estimated using the olivine-spinel geothermometer and varying the water content of the reconstructed melt, this method yields a water content of approximately 2.5 wt% for TIG-19-7748, 3 wt% for TIG-19-7858 and ~ 2.5 wt% for OXI-19-7720. These estimates differ somewhat from those obtained using the models of Gavrilenko et al. (2016) and (Portnyagin et al., 2019), but this almost certainly reflects the high uncertainty of the olivine-spinel geothermometer and the many assumptions made during the reconstruction of the melt compositions. Therefore, we conclude that the high-LREE melts of the TD contained approximately 1.5–3 wt% H_2O and the high-Mg melts of the MO contained 2–5.5 wt% H_2O.

The data indicate two distinct types of fluids: H_2O-Cl-rich and H_2O-Cl-poor. The high-LREE picrobasalts have high F/Cl ratios and relatively low water contents, as previously reported for high-Ti Holocene rocks of the Sredinny Range. This was due likely to the re-mobilization of fluids stored in the lithosphere (Nekrylov et al., 2021). In contrast, the H_2O-Cl-rich sample of high-Mg basalt from the MO is compositionally closer (and contains even more Cl) to the melt inclusions from the Akhtang and Ichinsky massifs, which are interpreted to represent the back-arc part of the modern subduction zone of Kamchatka (Churikova et al., 2007). It is a matter of debate whether the modern Pacific slab could have affected back-arc volcanism in the SR (e.g., Nekrylov et al., 2021). However, the dehydration of remnants of the Pacific slab subducted under the ancient SR subduction zone could be the source of these H_2O-Cl-rich melts.

5.3. The mineralogical composition of the source

The minor and trace element composition of primitive magmatic olivine has been shown to provide a signature for the mineralogical composition of the source (e.g., Herzberg, 2011; Sobolev et al., 2007). Olivine from some of the samples has a higher Ni content (Fig. 9a) and lower contents of Ca (Fig. 9b) and Mn (Fig. 9c) than olivine from the MORB. These features could reflect a dominantly pyroxenitic source for the magmas (e.g. Sobolev et al., 2007). However, the Ni and Ca contents of olivine can also be strongly affected by magma fractionation (e.g., Sato, 1977) and the H_2O activity in the melt (Gavrilenko et al., 2016), respectively. The three compositional parameters (Ni, Ca and Mn) are diagnostic only for part of the olivine population of the basalts of the MO. Some of the olivine crystals from the high-LREE picrobasalts of the TD are also depleted in Mn and Ca (Fig. 13) but their Ni content is relatively low.

It is noteworthy that both the TD high-LREE picrobasalts and the MO Mg basalts contain olivine that displays a wide range of composition (Fig. 13). For example, the olivine of samples OXI-19-7807 and OXI-19-7720 is almost evenly divided between “pyroxenitic” and “peridotitic” compositions. The olivine from high-LREE samples, TIG-19-7858 and TIG-19-7874, displays an even wider range of composition, from a nearly MORB-like high-Ca “peridotitic” composition to that of the pyroxenitic olivine from the MO (Fig. 12). These broad ranges of olivine composition may indicate a mixed peridotite-pyroxenite mantle source for the entire FZ that was melted under varying fluid regimes, with the environment being more H_2O-rich for the MO and less so for the TD.

5.4. The nature of LREE enrichment in picrobasalts

A particularly intriguing of the picrobasaltic rocks is their trace element enrichment and especially in the LREE. This characteristic is primary, as confirmed by the melt inclusions study. Compositions of MI from high-Mg olivines (Fo 88–90) from picrobasalts demonstrate the same LREE behavior (Figs. 6, 8).

Rocks that are LREE-enriched have been described in other volcanic provinces, i.e., in intraplate (Gao et al., 2008), back-arc (Ishizuka et al., 2010) and collisional settings (Neill et al., 2015; Sugden et al., 2019). In all cases, this enrichment was accompanied by elevated concentrations of other incompatible elements and very high La/Yb ratios and, in all cases, they have been interpreted to reflect the involvement of enriched lithospheric components. The high-LREE picrobasalts of the TD, however, demonstrate very unbalanced compositions with ultimate enrichment in the LREE part of the spectra and typical-island arc signatures for the other trace elements. This kind of trace element distribution cannot be explained by the melting of some certain type of mantle source(s). The LREE contents of the picrobasalts are too high to be explained by a depleted MORB-type source and the concentrations of the other HFSE are too low to be explained by an enriched OIB-type source or subcontinental lithospheric mantle. Additionally, the high LILE/HFSE ratios (Fig. 8), the elevated volatile contents (Fig. 11), and the oxygen fugacity of the melts (Fig. 12) leave little doubt that melting was fluid-induced.

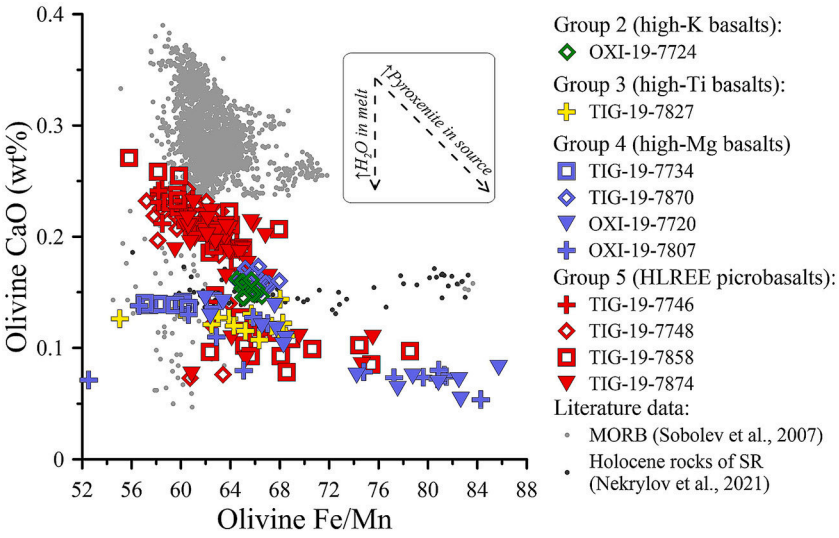

Fig. 13. A plot of the CaO content of olivine phenocrysts versus their Fe/Mn ratio. The corresponding compositions for MORB (Sobolev et al., 2007) and the Late Quaternary basalts of the SR (Nekrylov et al., 2021) are also shown for comparison.

Unusual LREE enrichment has also been reported for other supra-subduction and post-subduction volcanic rocks (e.g. Ishizuka et al., 2010; Sugden et al., 2019). However, even for supra-subduction rocks, the isotopic composition suggests that the lithosphere plays a role in magma genesis (Ishizuka et al., 2010). The lithospheric origin of the LREE enrichment in our case is consistent with a low Cl/F fluid source (Nekrylov et al., 2021) and the combination of a sulfur deficiency and copper enrichment (e.g., Richards, 2009). The actual process of LREE enrichment in such magmas, however, is still a subject of debate.

Campbell and Gorton (1980) proposed a model for the enrichment of LREE generated by the disequilibrium melting of LREE-rich accessory phases in the mantle. They argued that "such a phase will be among the first to melt and thus will dominate the REE profiles of early-formed liquids, even if subsequent partial re-equilibration occurs". Allanite may be a suitable candidate for this role, as it has been reported to be a carrier of LREE in the SZ (Hermann, 2002). Hermann (2002) proposed that a significant metasomatic mantle contribution of the LREE would only have been possible if the SZ liquid was extracted at high temperature. Simple modeling shows that <0.1 wt% of allanite (Hermann, 2002) in the source would be sufficient to provide the observed enrichment in the LREE without affecting the other incompatible elements. Although allanite may contain elevated concentrations of Th and U, the data illustrated in Fig. 9 of Hermann (2002) demonstrate that, in many cases, the concentration of these elements is relatively low. Consequently, therefore, their behavior in the resulting melt will not be influenced to such a degree as is observed for LREE. Amphibole and apatite also have been proposed as source for the LREE (Sugden et al., 2019).

5.5. *Controls on the remarkably widespread distribution of high-Mg rocks: A coupling of tectonic setting and a regional stress field?*

One of the most striking features of the FZ is the unusually widespread distribution of rocks with primitive compositions. In our previous studies of the volcanism of the SR, we have occasionally found high-Mg basalts (Volynets et al., 2010, 2018, 2020), but they were always represented by single cones or lava flows within large volcanic fields (as, for example, the high-Mg Enkavtenup cone in AD) and, in comparison to the medium-Mg rocks, are extremely rare. Never, to our knowledge, have high-Mg basalts been found in such long chains in such a large and wide zone as is the case for this FZ in the Sredinny Range. The presence of picrobasaltic rocks makes this finding unique not only for the SR but for the entire Quaternary volcanism of Kamchatka.

It is clear that many eruptive centers, including most of those with high-Mg basalts, in the studied area are confined to faults and chains of scoria cones located along the faults or fissures. The entire fault zone is considered presently active (Zelenin and Garipova, 2022), and it was active during the periods of eruptions, as the fault scarps either are covered by lava flows or deform the flows. The fault planes that are visible at the surface do not penetrate below the brittle-ductile boundary in the upper crust and therefore cannot serve as magma conduits for the entire depth of magma ascent (which, in the case of picrobasalts, may have started in the upper mantle), but may guide magma at the surface. If the fault zone has a volcano-tectonic nature and appears on the surface in response to processes occurring in the magmatic feeding system (so-called "magma fracking", e.g., Maimon et al., 2012, Mathieu et al., 2008, and many others), it may not extend far from the volcanic zone. Irrespective of the role of the fault zone, the stress field directly affects volcanism. Cembrano and Lara (2009) emphasized that crustal deformation may exert a fundamental control on magma differentiation, which, in turn, can determine the nature and composition of volcanism along and across continental margins. This notwithstanding, it has been shown that the stress field controlling magma ascent depends on the stress distribution inside the lithosphere and, in particular, the regional stress field and local stress barriers corresponding to rheological and/or structural discontinuities. In the case of monogenetic volcanism, the paths of magma migration are especially sensitive to changes in this stress field (Gómez-Vasconcelos et al., 2020; Martí et al., 2016 and references therein).

The area investigated in this study is the largest active FZ in the SR with an exceptional diversity of erupted product compositions, which appeared on the surface close in space and time. It records an unusually wide distribution of primitive end-members confined to the FZ. There are no direct data on the nature of the stress field at the time of magma ascent and eruption. However, all the normal faults that developed in the FZ have the same strike irrespective of the age of the deformed surface (Fig. 14). This information suggests that the fault zone emerged in a tectonic setting similar to that at present, after the docking of the Kronotsky arc terrane some 10–2 Ma, and reflects its location at the northern limit of modern crustal extension. According to K—Ar age data, volcanic activity in this part of the SR has been active since at least the Early Pliocene. The first dated episode of primitive magma eruption took place in the TD at 3.5 Ma. This was followed by a period of repose starting at 3.3 Ma that lasted approximately 2 Ma, while eruptions of medium- and high-K rocks took place in the MO and AD. The next major episode of high-Mg volcanism began in the TD at 1.5 Ma, with eruptions

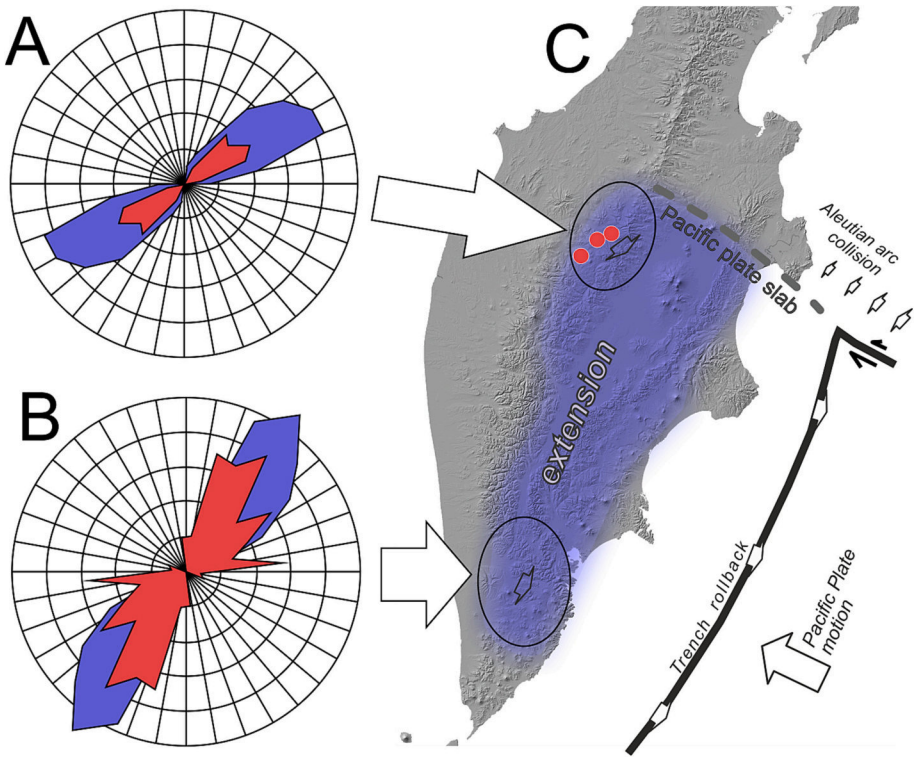

Fig. 14. Rose diagrams showing the strike of the normal faults and magma-transmitting fissures (A) in the Sredinny Range (Zelenin and Garipova, 2022) and (B) in Southern Kamchatka (Zelenin, 2017). A schematic map (C) shows the locations of the diagrams presented in A and B and the sites of the study (red circles) at the northern end of the Pacific slab and a tentative area of crustal extension (Zelenin and Garipova, 2022).

of picrobasalts and high-Mg basalts, and continued with the eruption of high-Mg rocks until about 0.3 Ma. Eruptions of medium-K, high-K and high-Ti basalts continued until the Late Pleistocene (<50 Ka).

Primitive magma eruptions in the TD are unlikely to have occurred above the normal subduction zone. Instead, these unusual eruptions that started at about 3.5 Ma marked the transition to rear-arc extension after the docking of the Kronotsky arc. Our findings raise the question of what is primary, cracking of the crust in response to the movement of magma or earthquake-induced faulting, leading to the rapid rise of primitive magma from greater depths. The widespread distribution of high-Mg rocks might be the product of the unusual coincidence of active regional tectonic and weakened zones in the crust, which allows primitive magmas to reach the surface, whereas in the other regions of the SR, because it is more difficult for the melts to break through, they either do not reach the surface or have sufficient time to fractionate significantly.

We believe that the case study presented in this paper provides an important example of the close interaction of local stresses, caused by magma migration through the crust, with a regional stress field, involving deeper levels of crust and upper mantle. We also believe that this interaction may have been a delayed response to the accretion of the Kronotsky and Kamchatsky Mys peninsulas (about 5 Ma and 2 Ma ago, respectively) during the accretion of the extinct Kronotsk arc to the Miocene-Pliocene Kamchatka arc system (Avdeiko et al., 2006; Lander and Shapiro, 2007; and others). The regional stress could have been both the trigger for the re-activation of a metasomatized lithosphere, causing extensive melting beneath the FZ, and the “icebreaker”, which paved the way for the ascent of the magma up a system of faults.

6. Conclusions

(1) The volcanic rocks from the active fault zone in the Sredinny Range of Kamchatka have a wide range of compositions, and include medium-K, moderate-Mg, high-K, high-Ti, high-Mg basalts and high-LREE picrobasalts. This level of diversity is quite unusual for monogenetic volcanic fields. The maximum extent of compositional variability is found within the Tigilsky Dol, where rocks of high-Mg composition are widespread along the FZ and are frequently confined to the faults. This is the first report of such a broad distribution of rocks of primitive composition in the SR.

(2) The main pulses of volcanic activity in the study area occurred at 4.3–3, 2, 1.5, 1 Ma, and from 0.3 to 0.05 Ma. Primitive rocks first appeared on the surface at 3.5 Ma. The massive expression of high-Mg volcanism took place at 1.5–1 and 0.3 Ma, and may have been connected to the formation of the FZ.

(3) Our findings include the first discovery of Quaternary picrobasaltic rocks in Kamchatka, as well as the first description of the disproportional LREE enrichment of primitive volcanic rocks in Kamchatka. Possible explanations for this phenomenon include disequilibrium melting of accessory allanite or metasomatic processes in the lithosphere.

(4) Based on the distribution of incompatible trace elements, the volatile content of the magmas and calculated oxygen fugacity values, the volcanism is attributed to fluid-induced melting of a depleted MORB-like mantle. The highest volatile concentrations and level of oxidation degree are recorded by olivine-hosted melt inclusions of the Mount Oxi massif, which is also the locus of the densest distribution of active faults in the area.

(5) Mineralogical data, e.g., the low-Ca, high-Ni and high-Fe/Mn of forsterite phenocrysts, indicate participation of a pyroxenitic source in the mantle melting. However, the co-existence of olivine crystals of “pyroxenitic” and “peridotitic” origin in the same samples suggests a mixed peridotite-pyroxenite source that melted under different fluid regimes (more water-rich in the case of the Mount Oxi massif). The Fo content of olivine phenocrysts reaches 93.2 mol%, which is the highest recorded Fo content for olivine in Quaternary Kamchatka basalts. Enrichment in the LREE and Cu and a deficiency in S of picrobasalts of the TD suggest that their source lithologies were lithospheric.

(6) The calculated crystallization temperatures (1111–1292 °C) and oxygen fugacity (ΔQFM +0.7 ± 2.0 log. units) provide constraints on the crystallization conditions in the back-arc of Kamchatka SZ. The volatile contents of the parental melts for the picrobasalts vary in a range previously reported for the Late Quaternary basalts of the Sredinny Range (Churikova et al., 2007; Nekrylov et al., 2021).

(7) Two fluid sources are interpreted to be involved in the genesis of the magmas of the Sredinny Range, namely the dehydrating remnants of the ancient Pacific slab (high H_2O and Cl/F) in the case of the Mount Oxi massif and lithospheric, amphibole-rich rocks (low H_2O and Cl/F) in case of picrobasalts of the Tigilsky Dol.

Declaration of Competing Interest

The authors declare that they have no known competing financial interests or personal relationships that could have influenced or appear to have influenced the research reported in this paper.

Data availability

All results obtained by this investigation, as well as the measurements of standards, are available in Supplementary Materials 1 (Tables S1– S3, whole rock data), and 2 (Tables S3–S8, compositions of olivine, spinel, and melt inclusions in olivine).

Acknowledgements

This research was performed in accordance with the research themes of IVS FEB RAS N⁰ 0282-2019-0004, GIN RAS N⁰ FMMG-2022-0002, IGEM RAS, GEOHI RAS, and with financial support from RFBR grants N⁰ 17-05-00112, 18-05-00224, 20-05-00085. The authors are grateful to V. Rodin, T. Karimov, A. Kurbatov, A. Burkova, A. Myasnikov, A. Kirilenko and L. Balibalova for their help and collaboration in the fieldworks. Special thanks to V. Karandashev and A. Yakushev for the analytical work, to D. Melnikov for his help with the preparation of Fig. 2 and to Prof. A.E. Williams-Jones for his enormous help with the language editing and improving the readability of the manuscript. Constructive reviews by Dr. Iain Neill and an anonymous referee helped us to improve the original version of this manuscript.

Appendix A. Supplementary data

Supplementary data to this article can be found online at https://doi.org/10.1016/j.lithos.2023.107306.

References

Almeev, R.R., Holtz, F., Koepke, J., Parat, F., Botcharnikov, R.E., 2007. The effect of H_2O on olivine crystallization in MORB: experimental calibration at 200 MPa. Am. Mineral. 92 (4), 670–674. https://doi.org/10.2138/am.2007.2484.

Avdeiko, G.P., Palueva, A.A., Khleborodova, O.A., 2006. Geodynamic conditions of volcanism and magma formation in the Kurile-Kamchatka island-arc system. Petrology 14 (3), 230–246. https://doi.org/10.1134/S0869591106030027.

Awdankiewicz, M., Rapprich, V., Mikova, J., 2016. Magmatic evolution of compositionally heterogeneous monogenetic Cenozoic Strzelin Volcanic Field (Fore-Sudetic Block, SW Poland). J. Geosci. 61 (4), 425–450. https://doi.org/10.3190/jgeosci.221.

Ballhaus, C., Berry, R.F., Green, D.H., 1991. High pressure experimental calibration of the olivine-orthopyroxene-spinel oxygen geobarometer: implications for the oxidation state of the upper mantle. Contrib. Mineral. Petrol. 107 (1), 27–40. https://doi.org/10.1007/BF00311183.

Bazanova, L.I., Pevzner, M.M., 2001. Khangar: one more active volcano in Kamchatka. Dokl. Earth Sci. 377A, 307–309 (In Russian).

Borisov, A.A., Shapkin, A.I., 1990. A new empirical equation rating Fe3+/Fe2+ in magmas to their composition, oxygen fugacity, and temperature. Geochem. Int. 27 (1), 111–116.

Campbell, I.H., Gorton, M.P., 1980. Accessory phases and the generation of LREE-enriched basalts – a test for disequilibrium melting. Contrib. Mineral. Petrol. 72, 157–163. https://doi.org/10.1007/BF00399475.

Cembrano, J., Lara, L., 2009. The link between volcanism and tectonics in the southern volcanic zone of the Chilean Andes: a review. Tectonophysics 471 (1–2), 96–113. https://doi.org/10.1016/j.tecto.2009.02.038.

Churikova, T., Dorendorf, F., Wörner, G., 2001. Sources and fluids in the mantle wedge below Kamchatka, evidence from across-arc geochemical variation. J. Petrol. 42 (8), 1567–1593. https://doi.org/10.1093/petrology/42.8.1567.

Churikova, T., Wörner, G., Mironov, N., Kronz, A., 2007. Volatile (S, Cl and F) and fluid mobile trace element compositions in melt inclusions: Implications for variable fluid sources across the Kamchatka arc. Contrib. Mineral. Petrol. 154, 217–239. https://doi.org/10.1007/s00410-007-0190-z.

Churikova, T.G., Gordeychik, B.N., Iwamori, H., Nakamura, H., Ishizuka, O., Nishizawa, T., Haraguchi, S., Miyazaki, T., Vaglarov, B., 2015. Petrological and geochemical evolution of the Tolbachik volcanic massif, Kamchatka, Russia. J. Volcanol. Geotherm. Res. 307, 156–181. https://doi.org/10.1016/j.jvolgeores.2015.10.026.

Connor, C.B., Conway, F.M., Sigurdsson, H., 2000. Basaltic Volcanic Fields: Encyclopedia of volcanoes, pp. 331–343.

Coogan, L.A., Saunders, A.D., Wilson, R.N., 2014. Aluminum-in-olivine thermometry of primitive basalts: evidence of an anomalously hot mantle source for large igneous provinces. Chem. Geol. 368, 1–10. https://doi.org/10.1016/j.chemgeo.2014.01.004.

Danyushevsky, L.V., Plechov, P., 2011. Petrolog3: Integrated software for modeling crystallization processes. Geochem. Geophys. Geosyst. 12 (7) https://doi.org/10.1029/2011GC003516.

Danyushevsky, L.V., Della-Pasqua, F.N., Sokolov, S., 2000. Re-equilibration of melt inclusions trapped by magnesian olivine phenocrysts from subduction-related magmas: petrological implications. Contrib. Mineral. Petrol. 138 (1), 68–83. https://doi.org/10.1007/PL00007664.

Dirksen, O.V., 2009. Late Quaternary Areal Volcanism in Kamchatka (structural confinement, geological-geomorphological effect, space-time regularities), PhD thesis, St.Petersburg, 18 p. (In Russian).

Duggen, S., Portnyagin, M., Baker, J., Ulfbeck, D., Hoernle, K., Garbe-Schönberg, D., Grassineau, N., 2007. Drastic shift in lava geochemistry in the volcanic-front to rear-arc region of the Southern Kamchatkan subduction zone: evidence for the transition from slab surface dehydration to sediment melting. Geochim. Cosmochim. Acta 71 (2), 452–480. https://doi.org/10.1016/j.gca.2006.09.018.

Fischer, T.P., 2008. Fluxes of volatiles (H_2O, CO_2, N_2, Cl, F) from arc volcanoes. Geochem. J. 42, 21–38. https://doi.org/10.2343/geochemj.42.21.

Ford, C.E., Russell, D.G., Craven, J.A., Fisk, M.R., 1983. Olivine-liquid equilibria: temperature, pressure and composition dependence of the crystal/liquid cation partition coefficients for Mg, Fe2+, Ca and Mn. J. Petrol. 24 (3), 256–266. https://doi.org/10.1093/petrology/24.3.256.

Gao, S., Rudnick, R.L., Xu, W.L., Yuan, H.L., Liu, Y.S., Walker, R.J., Puchtel, I.S., Liu, X., Huang, H., Wang, X.R., Yang, J., 2008. Recycling deep cratonic lithosphere and generation of intraplate magmatism in the North China Craton. Earth Planet. Sci. Lett. 270 (1–2), 41–53. https://doi.org/10.1016/j.epsl.2008.03.008.

Gavrilenko, M., Herzberg, C., Vidito, C., Carr, M.J., Tenner, T., Ozerov, A., 2016. A calcium-in-olivine geohygrometer and its application to subduction zone magmatism. J. Petrol. 57, 1811–1832. https://doi.org/10.1093/petrology/egw062.

Gómez-Vasconcelos, M.G., Macías, J.L., Avellán, D.R., Sosa-Ceballos, G., Garduño-Monroy, V.H., Cisneros-Máximo, G., Layer, P.W., Benowitz, J., López-Loera, H., López, F.M., Perton, M., 2020. The control of preexisting faults on the distribution, morphology, and volume of monogenetic volcanism in the Michoacán-Guanajuato Volcanic Field. GSA Bull. 132 (11−12), 2455–2474. https://doi.org/10.1130/B35397.1.

Gorbach, N.V., Portnyagin, M.V., 2011. Geology and petrology of the lava complex of young Shiveluch volcano, Kamchatka. Petrology 19, 134–166. https://doi.org/10.1134/S0869591111020068.

Gorbach, N.V., Nekrylov, N., Portnyagin, M.V., Hoernle, K., 2023. New data on the composition of rocks and minerals from Kharchinsky and Zarechny volcanoes (Central Kamchatka Depression): heterogeneity of mantle source and features of the magma evolution in crustal conditions. Petrology 31 (3), 320–337. https://doi.org/10.1134/S0869591123030050.

Gorbatov, A., Kostoglodov, V., Suarez, G., Gordeev, E., 1997. Seismicity and structure of the Kamchatka subduction zone. J. Geophys. Res. 102 (B8), 17883–17898. https://doi.org/10.1029/96JB03491.

Hermann, J., 2002. Allanite: thorium and light rare earth element carrier in subducted crust. Chem. Geol. 192, 289–306. https://doi.org/10.1016/S0009-2541(02)00222-X.

Herzberg, C., 2011. Identification of source lithology in the Hawaiian and Canary Islands: implications for origins. J. Petrol. 52 (1), 113–146. https://doi.org/10.1093/petrology/egr012.

Ishizuka, O., Yuasa, M., Tamura, Y., Shukuno, H., Stern, R.J., Naka, J., Joshima, M., Taylor, R.N., 2010. Migrating shoshonitic magmatism tracks Izu – Bonin – Marianaintra-oceanic arc rift propagation. Earth Planet. Sci. Lett. 294 (1–2), 111–122. https://doi.org/10.1016/j.epsl.2010.03.016.

Kepezhinskas, P., Mcdermott, F., Defant, M.J., Hochstaedter, A., Drummond, M.S., Hawkesworth, C.J., Koloskov, A.V., Maury, R.C., Bellon, H., 1997. Trace element and Sr-Nd-Pb isotopic constraints on a three-component model of Kamchatka Arc petrogenesis. Geochim. Cosmochim. Acta 61 (3), 577–600. https://doi.org/10.1016/S0016-7037(96)00349-3.

Koloskov, A.V., Flerov, G.B., Perepelov, A.B., Melekestsev, I.V., Puzankov, M.Yu., Filosofova, T.M., 2013. The evolutionary stages and petrology of the Kekuknai volcanic massif reflecting the magmatism in the backarc zone of the Kuril-Kamchatka island arc system. Part II. Petrologic and mineralogical features, petrogenesis model. J. Volcanol. Seismol. 7, 145–169. https://doi.org/10.1134/S0742046313020048.

Konstantinovskaia, E.A., 2001. Arc–continent collision and subduction reversal in the Cenozoic evolution of the Northwest Pacific: an example from Kamchatka (NE

Russia). Tectonophysics 333 (1–2), 75–94. https://doi.org/10.1016/S0040-1951(00)00268-7.
Korneeva, A., Kamenetsky, V.S., Nekrylov, N., Kontonikas-Charos, A., Kamenetsky, M., Savelyev, D., Zelenski, M., Krasheninnikov, S., 2023. A melt inclusion approach to reconstructing sulfur contents and sulfide saturation of primitive basaltic melts. Lithos 436–437, 106956. https://doi.org/10.1016/j.lithos.2022.106956.
Kozhurin, A., Zelenin, E., 2017. An extending island arc: the case of Kamchatka. Tectonophysics 706, 91–102. https://doi.org/10.1016/j.tecto.2017.04.001.
Krykun, N.F., Litvinov, A.F., Sidorenko, V.I., 2020. State geological map of Russian Federation. Scale 1: 200 000. Second edition. Series West-Kamchatka. O-57-XXXIV (Kozyrevsk), Explanatory note. VSEGEI, St. Petersburg.
Kutyrev, A.V., Kamenetsky, V.S., Park, J.W., Maas, R., Demonterova, E.I., Antsiferova, T. N., Ivanov, A.V., Hwang, J., Abersteiner, A., Ozerov, A.Y., 2021. Primitive high-K intraoceanic arc magmas of Eastern Kamchatka: Implications for Paleo-Pacific tectonics and magmatism in the Cretaceous. Earth Sci. Rev. 220, 103703 https://doi.org/10.1016/j.earscirev.2021.103703.
Lander, A.V., Shapiro, M.N., 2007. The origin of the modern Kamchatka subduction zone. In: Eichelberger, J., Gordeev, E., Izbekov, P., Kasahara, M., Lees, J. (Eds.), Geophysical Monograph Series, pp. 57–64. https://doi.org/10.1029/172GM05.
Laverov, N.P. (Ed.), 2005. Modern and Holocene Volcanism in Russia. Nauka, Moscow (604 p).
Le Corvec, N., Spörli, K.B., Rowland, J., Lindsay, J., 2013. Spatial distribution and alignments of volcanic centers: clues to the formation of monogenetic volcanic fields. Earth Sci. Rev. 124, 96–114. https://doi.org/10.1016/j.earscirev.2013.05.005.
Lloyd, A.S., Plank, T., Ruprecht, P., Hauri, E.H., Rose, W., 2013. Volatile loss from melt inclusions in pyroclasts of differing sizes. Contrib. Mineral. Petrol. 165 (1), 129–153. https://doi.org/10.1007/s00410-012-0800-2.
Maimon, O., Lyakhovsky, V., Melnik, O., Navon, O., 2012. The propagation of a dyke driven by gas-saturated magma. Geophys. J. Int. 189 (2), 956–966. https://doi.org/10.1111/j.1365-246X.2012.05342.x.
Martí, J., López, C., Bartolini, S., Becerril, L., Geyer, A., 2016. Stress controls of monogenetic volcanism: a review. Front. Earth Sci. 4, 106. https://doi.org/10.3389/feart.2016.00106.
Mathieu, L., van Wyk de Vries, B., Holohan, E.P., Troll, V.R., 2008. Dykes, cups, saucers and sills: Analogue experiments on magma intrusion into brittle rocks. Earth Planet. Sci. Lett. 271 (1–4), 1–13. https://doi.org/10.1016/j.epsl.2008.02.020.
McDonough, W.F., Sun, S.-S., 1995. The composition of the Earth. Chem. Geol. 120 (3–4), 223–253. https://doi.org/10.1016/0009-2541(94)00140-4.
Neill, I., Meliksetian, K., Allen, M.B., Navasardyan, G., Kuiper, K., 2015. Petrogenesis of mafic collision zone magmatism: the Armenian sector of the Turkish-Iranian Plateau. Chem. Geol. 403, 24–41. https://doi.org/10.1016/j.chemgeo.2015.03.013.
Nekrylov, N.A., Plechov, P.Y., Bychkov, K.A., Perepelov, A.B., Puzankov, M.Y., Shur, M. Y., Dirksen, O.V., Bazanova, L.I., 2015. Parental melts of the last volcanic pulse in the Sedanka field, Sredinny Range, Kamchatka. Mosc. Univ. Geol. Bull. 70, 233–239. https://doi.org/10.3103/S0145875215030060.
Nekrylov, N., Portnyagin, M.V., Kamenetsky, V.S., Mironov, N.L., Churikova, T.G., Plechov, P.Y., Abersteiner, A., Gorbach, N.V., Gordeychik, B.N., Krasheninnikov, S. P., Tobelko, D.P., Shur, M.Y., Tetroeva, S.A., Volynets, A.O., Hoernle, K., Wörner, G., 2018a. Chromium spinel in late Quaternary volcanic rocks from Kamchatka: Implications for spatial compositional variability of subarc mantle and its oxidation state. Lithos 322, 212–224. https://doi.org/10.1016/j.lithos.2018.10.011.
Nekrylov, N.A., Popov, D.V., Plechov, P.Y., Shcherbakov, V.D., Danyushevsky, L.V., Dirksen, O.V., 2018b. Garnet-pyroxenite-derived end-member magma type in Kamchatka: evidence from composition of plivine and olivine-hosted melt inclusions in Holocene rocks of Kekuknaisky volcano. Petrology 26, 329–350. https://doi.org/10.1134/S0869591118040057.
Nekrylov, N., Popov, D.V., Plechov, P.Y., Shcherbakov, V.D., Danyushevsky, L.V., 2021. The origin of the Late Quaternary back-arc volcanic rocks from Kamchatka: evidence from the compositions of olivine and olivine-hosted melt inclusions. Contrib. Mineral. Petrol. 176 (9), 71. https://doi.org/10.1007/s00410-021-01830-4.
Nekrylov, N., Kamenetsky, V.S., Savelyev, D.P., Gorbach, N.V., Kontonikas-Charos, A., Palesskii, S.V., Shcherbakov, V.D., Kutyrev, A.V., Savelyeva, O.L., Korneeva, A.A., Kozmenko, O.A., Zelenski, M.E., 2022. Platinum-group elements in Late Quaternary high-Mg basalts of eastern Kamchatka: evidence for minor cryptic sulfide fractionation in primitive arc magmas. Lithos 412–413. https://doi.org/10.1016/j.lithos.2022.106608.
Németh, K., Kereszturi, G., 2015. Monogenetic volcanism: personal views and discussion. Int. J. Earth Sci. 104, 2131–2146. https://doi.org/10.1007/s00531-015-1243-6.
Nishizawa, T., Nakamura, H., Churikova, T., Gordeychik, B., Ishizuka, O., Haraguchi, S., Miyazaki, T., Vaglarov, B.S., Chang, Q., Hamada, M., Kimura, J.I., Ueki, K., Toyama, C., Nakao, A., Iwamori, H., 2017. Genesis of ultra-high-Ni olivine in high-Mg andesite lava triggered by seamount subduction. Sci. Rep. 7 https://doi.org/10.1038/s41598-017-10276-3.
Ogorodov, N.V., Kozhemyaka, N.N., Vazheevskaya, A.A., Ogorodova, A.S., 1972. Volcanoes and Quaternary Volcanism of the Sredinny Range of Kamchatka. Nauka, Moscow, 190 p. (In Russian).
Pevzner, M.M., 2004. The first geological data on the chronology of Holocene eruptive activity in the Ichinskii volcano (Sredinnyi Ridge, Kamchatka). Dokl. Earth Sci. 395 (3), 335–337.
Pevzner, M.M., 2015. Holocene Volcanism of Sredinny Range of Kamchatka. Transactions of the Geological Institute, vol. 608. GEOS, M.A. Moscow. Resp.ed. Fedonkin. 252 p. (In Russian).
Pevzner, M.M., Lebedev, V.A., Kuscheva, Y.V., Volynets, A.O., Tolstykh, M.L., Babansky, A.D., 2020. Early Quaternary age of the final stage of volcanism in the central part of the Sredinny Range of Kamchatka (K–Ar Data). Dokl. Earth Sci. 490, 1–3. https://doi.org/10.1134/S1028334X20010080.
Porter, C., Morin, P., Howat, I., Noh, M.-J., Bates, B., Peterman, K., Keesey, S., Schlenk, M., Gardiner, J., Tomko, K., Willis, M., Kelleher, C., Cloutier, M., Husby, E., Foga, S., Nakamura, H., Platson, M., Wethington Jr., M., Williamson, C., Bauer, G., Enos, J., Arnold, G., Kramer, W., Becker, P., Doshi, A., D'Souza, C., Cummens, P., Laurier, F., Bojesen, M., 2018. ArcticDEM, Version 3. https://doi.org/10.7910/DVN/OHHUKH. Harvard Dataverse, V1.
Portnyagin, M., Bindeman, I., Hoernle, K., Hauff, F., 2007. Geochemistry of primitive lavas of the Central Kamchatka Depression: Magma generation at the edge of the Pacific Plate. In: Eichelberger, J., Gordeev, E., Izbekov, P., Kasahara, M., Lees, J. (Eds.), Volcanism and Subduction: The Kamchatka Region, pp. 199–239. https://doi.org/10.1029/172GM16.
Portnyagin, M., Almeev, R., Matveev, S., Holtz, F., 2008. Experimental evidence for rapid water exchange between melt inclusions in olivine and host magma. Earth Planet. Sci. Lett. 272 (3–4), 541–552. https://doi.org/10.1016/j.epsl.2008.05.020.
Portnyagin, M., Duggen, S., Hauff, F., Mironov, N., Bindeman, I., Thirlwall, M., Hoernle, K., 2015. Geochemistry of the late Holocene rocks from the Tolbachik volcanic field, Kamchatka: towards quantitative modeling of subduction-related open magmatic systems. J. Volcanol. Geotherm. Res. 307, 133–155. https://doi.org/10.1016/j.jvolgeores.2015.08.015.
Portnyagin, M., Mironov, N., Botcharnikov, R., Gurenko, A., Almeev, R.R., Luft, C., Holtz, F., 2019. Dehydration of melt inclusions in olivine and implications for the origin of silica-undersaturated island-arc melts. Earth Planet. Sci. Lett. 517, 95–105. https://doi.org/10.1016/j.epsl.2019.04.021.
Rasoazanamparany, C., Widom, E., Valentine, G.A., Smith, E.I., Cortes, J.A., Kuentz, D., Johnsen, R., 2015. Origin of chemical and isotopic heterogeneity in a mafic, monogenetic volcanic field: a case study of the Lunar Crater volcanic field, Nevada. Chem. Geol. 397, 76–93. https://doi.org/10.1016/j.chemgeo.2015.01.004.
Richards, J.P., 2009. Postsubduction porphyry Cu-Au and epithermal Au deposits: Products of remelting of subduction-modified lithosphere. Geology 37 (3), 247–250. https://doi.org/10.1130/G25451A.1.
Sato, H., 1977. Nickel content of basaltic magmas: identification of primary magmas and a measure of the degree of olivine fractionation. Lithos 10 (2), 113–120. https://doi.org/10.1016/0024-4937(77)90037-8.
Schellart, W.P., Freeman, J., Stegman, D.R., Moresi, L., May, D., 2007. Evolution and diversity of subduction zones controlled by slab width. Nature 446 (7133), 308–311. https://doi.org/10.1038/nature05615.
Shimizu, K., Saal, A.E., Myers, C.E., Nagle, A.N., Hauri, E.H., Forsyth, D.W., Kamenetsky, V.S., Niu, Y., 2016. Two-component mantle melting-mixing model for the generation of mid-ocean ridge basalts: Implications for the volatile content of the Pacific upper mantle. Geochim. Cosmochim. Acta 176, 44–80. https://doi.org/10.1016/j.gca.2015.10.033.
Smith, I.E., Brenna, M., Cronin, S.J., 2021. The magma source of small-scale intraplate monogenetic volcanic systems in northern New Zealand. J. Volcanol. Geotherm. Res. 418, 107326 https://doi.org/10.1016/j.jvolgeores.2021.107326.
Sobolev, A.V., Hofmann, A.W., Kuzmin, D.V., Yaxley, G.M., Arndt, N.T., Chung, S.L., Danyushevsky, L.V., Elliott, T., Frey, F.A., Garcia, M.O., Gurenko, A.A., Kamenetsky, V.S., Kerr, A.C., Krivolutskaya, N.A., Matvienkov, V.V., Nikogosian, I. K., Rocholl, A., Sigurdsson, I.A., Sushchevskaya, N.M., Teklay, M., 2007. The amount of recycled crust in sources of mantle-derived melts. Science 316 (5823), 412–417. https://doi.org/10.1126/science.1138113.
Sobolev, A., Asafov, E., Gurenko, A., Arndt, N.T., Batanova, V.G., Portnyagin, M.V., Garbe-Schönberg, D., Krasheninnikov, S.P., 2016. Komatiites reveal a hydrous Archaean deep-mantle reservoir. Nature 531, 628–632. https://doi.org/10.1038/nature17152.
Sugden, P.J., Savov, I.P., Wilson, M., Meliksetian, K., Navasardyan, G., Halama, R., 2019. The Thickness of the Mantle Lithosphere and Collision-Related Volcanism in the Lesser Caucasus. J. Petrol. 60 (2), 199–230. https://doi.org/10.1093/petrology/egy111.
Sun, S.S., McDonough, W.F., 1989. Chemical and isotopic systematics of oceanic basalts; implications for mantle composition and processes. In: Saunders, A.D., Norry, M.J. (Eds.), Magmatism in the Ocean Basins. Geological Society of London Special Publications, pp. 313–345. https://doi.org/10.1144/GSL.SP.1989.042.01.19.
Uslular, G., Gençalioğlu-Kuşcu, G., 2019. Mantle source heterogeneity in monogenetic basaltic systems: a case study of Eğrikuyu monogenetic field (Central Anatolia, Turkey). Geosphere 15 (2), 295–323. https://doi.org/10.1130/GES01682.1.
Venugopal, S., Schiavi, F., Moune, S., Bolfan-Casanova, N., Druitt, T., Williams-Jones, G., 2020. Melt inclusion vapour bubbles: the hidden reservoir for major and volatile elements. Sci. Rep. 10 (1), 1–14. https://doi.org/10.1038/s41598-020-65226-3.
Volynets, O.N., 1994. Geochemical Types, Petrology, and Genesis of Late Cenozoic Volcanic Rocks from the Kurile-Kamchatka Island-Arc System. Int. Geol. Rev. 36, 373–405. https://doi.org/10.1080/00206819409465467.
Volynets, A.O., Churikova, T.G., Wörner, G., Gordeychik, B.N., Layer, P., 2010. Mafic Late Miocene-Quaternary volcanic rocks in the Kamchatka back arc region: implications for subduction geometry and slab history at the Pacific-Aleutian junction. Contrib. Mineral. Petrol. 159 https://doi.org/10.1007/s00410-009-0447-9.
Volynets, A.O., Pevzner, M.M., Tolstykh, M.L., Babansky, A.D., 2018. Volcanism of the southern part of the Sredinny Range of Kamchatka in the Neogene-Quaternary. Russ. Geol. Geophys. 59 https://doi.org/10.1016/j.rgg.2018.12.004.
Volynets, A.O., Pevzner, M.M., Lebedev, V.A., Kuscheva, Y.V., Gol'tsman, Y.V., Kostitsin, Y.A., Tolstykh, M.L., Babansky, A.D., 2020. Stages of volcanic activity on the southeastern flank of the Sredinny range (Kamchatka): age, geochemistry, and isotopic characteristics of volcanic rocks of the Akhtang and Kostina mountain massifs. Russ. Geol. Geophys. 61 https://doi.org/10.15372/RGG2019158.

Zelenin, E.A., 2017. Late Quaternary deformations of Southern Kamchatka. Bulletin of Kamchatka Regional Association Educational-Scientific Center. Earth Sci. 35, 103–111. http://www.kscnet.ru/journal/kraesc/article/view/147.

Zelenin, E.A., Garipova, S.T., 2022. Active faulting in Sredinny Range, Kamchatka peninsula. Bulletin of Kamchatka Regional Association Educational-Scientific Center. Earth Sci. 53, 104–112. https://doi.org/10.31431/1816-5524-2022-1-53-104-112.

Zelenski, M., Kamenetsky, V.S., Nekrylov, N., Kontonikas-Charos, A., 2022. High sulfur in primitive arc magmas, its origin and implications. Minerals 12. https://doi.org/10.3390/min12010037.

Zhao, L., Liu, X., Zhao, D., Wang, X., Qiao, Q., 2021. Mapping the Pacific slab edge and toroidal mantle flow beneath Kamchatka. J. Geophys. Res. Solid Earth 126. https://doi.org/10.1029/2021JB022518 e2021JB022518.